Use of the Parcel Buoyancy Minimum (B_{min}) to Diagnose Simulated Thermodynamic Destabilization. Part II: Composite Analysis of Mature MCS Environments

STANLEY B. TRIER, CHRISTOPHER A. DAVIS, DAVID A. AHIJEVYCH, AND KEVIN W. MANNING

National Center for Atmospheric Research, Boulder, Colorado*

(Manuscript received 21 August 2013, in final form 23 October 2013)

ABSTRACT

Herein, the parcel buoyancy minimum (B_{min}) defined in Part I of this two-part paper is used to examine physical processes influencing thermodynamic destabilization in environments of mature simulated mesoscale convective systems (MCSs). These convection-permitting simulations consist of twelve 24-h forecasts during two 6-day periods characterized by two different commonly occurring warm-season weather regimes that support MCSs over the central United States.

A composite analysis of 22 MCS environments is performed where cases are stratified into surface-based (SB), elevated squall (ES), and elevated nonsquall (ENS) categories. A gradual reduction of lower-tropospheric B_{min} to values indicative of small convection inhibition, occurring over horizontal scales >100 km from the MCS leading edge, is a common aspect of each category. These negative buoyancy decreases are most pronounced for the ES and ENS environments, in which convective available potential energy (CAPE) is greatest for air parcels originating above the surface. The implication is that the vertical structure of the mesoscale environment plays a key role in the evolution and sustenance of convection long after convection initiation and internal MCS circulations develop, particularly in elevated systems.

Budgets of B_{min} forcing are computed for the nocturnally maturing ES and ENS composites. Though warm advection occurs through the entire 1.5-km-deep layer comprising the vertical intersection of the largest environmental CAPE and smallest environmental B_{min} magnitude, the net effect of terms involving vertical motion dominate the destabilization in both composites. These effects include humidity increases in air parcels due to vertical moisture advection and the adiabatic cooling of the environment above.

1. Introduction

Mesoscale convective systems (MCSs), defined here as any collection of deep, moist convective cells collectively having a diameter of a few hundred kilometers or more, typically initiate in thermodynamic environments of significant convective available potential energy (CAPE) and reduced convective inhibition (CIN, Colby 1984). In Part I of this paper, Trier et al. (2014) used the minimum buoyancy (B_{min}) of air parcels originating from different model vertical grid points to characterize susceptibility to convection in case studies of MCS initiation. In Part I the parcel buoyancy minimum, expressed in temperature units [$B_{min} = \min(T_{vp} - T_{ve})$], is the minimum (i.e., most negative) virtual temperature difference between a vertically displaced air parcel and its environment below 500 hPa.

Part I found that the local evolution of B_{min} was qualitatively similar to that of CIN. However, they noted that B_{min} was more amenable for use in budget calculations that estimate the forcing of its evolution since with B_{min} such calculations do not require vertical integration. Calculating B_{min} budgets for a given parcel origination level (see section 4 in Part I) requires knowledge of the forcing for thermodynamic changes at only this parcel origination level and for the environment at a level approximating where the lifted parcel attains its minimum buoyancy.

Applying this technique in case studies of the onset of convection initiation (CI) associated with subsequent MCSs, Part I found that vertical motions were important in reducing the negative buoyancy for cases ranging from nocturnal elevated convection near fronts to daytime

*The National Center for Atmospheric Research is sponsored by the National Science Foundation.

Corresponding author address: Stanley B. Trier, National Center for Atmospheric Research, P.O. Box 3000, Boulder, CO 80307-3000. E-mail: trier@ucar.edu

DOI: 10.1175/MWR-D-13-00273.1

surface-based initiation where surface fluxes were also crucial. In the current paper we use a composite approach to analyze the spatial distribution of B_{min} and the effects of mesoscale forcing on B_{min} in environments of different types of simulated *mature* MCSs.

Climatological studies using radar and rawinsonde data have linked MCS structure, movement, and longevity to aspects of their thermodynamic and kinematic environments in widely varying locations ranging from continental midlatitudes (e.g., Bluestein and Jain 1985; Houze et al. 1990) to the oceanic tropics (e.g., Barnes and Sieckman 1984; LeMone et al. 1998). However, the limited spatial and temporal resolution of rawinsonde data has not afforded routine, reliable diagnoses of the dynamics resulting in these important environmental characteristics.

The advent of convection-permitting numerical weather prediction (NWP) models has resulted in improvements in the fidelity of simulations of deep, organized convection (e.g., Schwartz et al. 2009). Thus, we may exploit the dynamical consistency and high resolution of these simulations to gain insights into how changes, including the reduction of convection inhibition, or specifically B_{min}, might proceed in actual MCS environments.

Environmental mesoscale forcing was a consistent factor in reducing the B_{min} to negligibly small magnitudes during the early initiation stages of MCSs in Part I. However, its importance is less obvious in some situations after the incipient convection has organized upscale. For example, in propagating squall lines, which are a common type of MCS, the interaction of the environmental vertical shear with the horizontal vorticity along the downshear edge of the storm-produced cold pool (Rotunno et al. 1988, hereafter RKW) engenders much stronger and more highly localized lifting than that typically found in the environment ahead of the MCS. Given sufficient CAPE, strong forced lifting along the MCS surface outflow, which is most common in environments with moderate-to-strong vertical shear, could allow MCS convection to persist without the necessity for larger-scale processes to reduce the magnitudes of B_{min} or CIN to negligible values in the environment.

Squall-type organization is favored in vertically sheared environments with near-neutral boundary layers that allow moist downdrafts that easily penetrate to the surface and produce a storm-induced cold pool. However, a significant fraction of midlatitude MCSs mature overnight poleward of surface fronts (e.g., Kane et al. 1987). These environments feature highly stratified near-surface conditions, which contrast with the conditions in typical squall-line environments. Fritsch and Forbes (2001) recognized this dichotomy in MCS environments and the implications it has for differences in organization and behavior among corresponding MCS types and proposed an MCS classification scheme based on these considerations. In particular, they emphasized the importance of large-scale frontal lifting in their type-1 MCSs, which given moist upstream conditions can be sufficient to saturate conditionally unstable air parcels, thus facilitating the sustenance of deep convection. Recent research has also indicated more intense and localized lifting in MCSs occurring in environments akin to the type-1 MCS environment, including quasi-stationary diabatically forced gravity waves that localize the strongest convection in some heavy rain-producing MCSs (e.g., Schumacher and Johnson 2008). The type-2 MCSs of Fritsch and Forbes (2001) occur in less baroclinic environments and are more likely to exhibit squall-type behaviors. These include downshear propagation with strong localized lifting near the leading edge of their evaporatively driven outflows, as in RKW.

Though it is not clear that lower-tropospheric B_{min} changes resulting from persistent mesoscale environmental forcing are by themselves capable of sustaining most MCSs, they can provide important thermodynamic preconditioning for locations in the path of MCSs. For example, horizontal temperature advection and vertical motion have been well documented (e.g., Maddox 1983; Cotton et al. 1989) in the environments of larger MCSs, termed mesoscale convective complexes (MCCs; Maddox 1980). An important objective of the current study is to illustrate how these and other mesoscale physical processes can directly affect lower-tropospheric negative buoyancy in the environment of the MCS. The mature MCS environment often contains important and persistent features, including surface fronts and the nocturnal low-level jet (LLJ), but may also be influenced by the upstream effects of organized convection, which have been found in idealized simulations with horizontally homogeneous initial conditions (e.g., Fovell 2002; Parker and Johnson 2004).

The simulated MCSs that are used in the composite analyses in this paper are selected from two different 6-day periods where frequent convective activity occurred over the central United States. These convectively active periods happened during contrasting large-scale regimes (section 2), thus permitting a reasonable number of cases from disparate warm-season MCS environments. The numerical model and the design of the simulations (described in Part I) are summarized in section 3, where we also provide verification of the general characteristics of the simulated precipitation. The procedures used for MCS case selection and compositing of their environments are discussed in section 4. Distributions of B_{min} and other thermodynamic and kinematic quantities for the different composites and

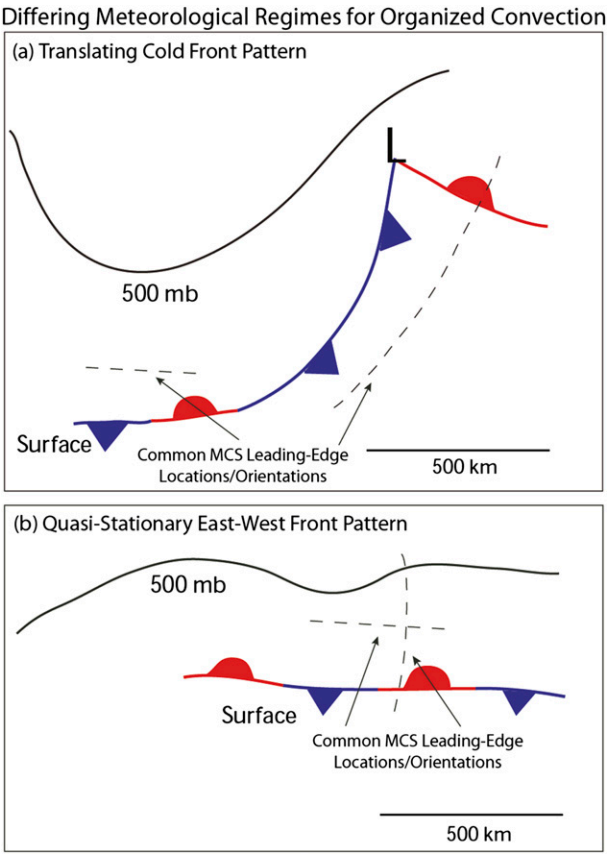

FIG. 1. Schematic diagram illustrating different synoptic environments associated with MCSs. Solid black curves indicate a 500-hPa geopotential height contour and curves with barbed and half-circle symbols represent surface fronts. The dashed lines indicate typical MCS locations and leading-edge orientations within these large-scale weather patterns.

the vertical structure of composite thermodynamic quantities and related forcing terms in the MCS environment are presented in section 5. The effects of the forcing on the evolution of $B_{\min}$ in the MCS environment are quantified in section 6 using local budget calculations.

2. The 10–16 June 2002 and 3–9 July 2003 MCS activity in the central United States

Two common large-scale patterns supporting warm-season MCS activity in the central United States are illustrated in Fig. 1. The pattern in Fig. 1a consists of a translating large-amplitude midtropospheric trough and associated surface cold front. The contrasting pattern in Fig. 1b has an east–west-oriented quasi-stationary surface front located underneath anticyclonic midtropospheric conditions with a weak embedded short-wave disturbance. These distinct large-scale patterns are similar to the ''synoptic'' (Fig. 1a) and ''frontal'' (Fig. 1b) heavy-rainfall patterns of Maddox et al. (1979). The dashed lines in Fig. 1 represent typical positions of MCSs with respect to these large-scale features. MCSs occurring ahead of the front in the synoptic MCS pattern (Fig. 1a) typically have squall-type characteristics akin to those of the Fritsch and Forbes (2001) type-2 MCS. MCSs occurring north of quasi-stationary fronts in the frontal MCS pattern are often aligned along the front and have characteristics of the Fritsch and Forbes (2001) type-1 MCS. However, MCSs in this large-scale pattern may also be oriented normal to the front (Fig. 1b). In this latter case significant low-level vertical shear oriented normal to the temperature gradient, which may be inferred from thermal wind considerations, is a strong organizing influence. Given sufficient CAPE, this hybrid of type-1 and -2 MCSs, recognized by Fritsch and Forbes (2001), can evolve into intense derecho MCSs (e.g., Johns and Hirt 1987).

The two 6-day periods selected for 0–24-h simulations in this paper encompass the different patterns of Fig. 1. The 10–15 June 2002 period during the International H_2O Project (IHOP; Weckwerth et al. 2004) conforms well in a time-averaged sense to the pattern in Fig. 1a (Sun et al. 2012, their Fig. 1). Stage-4 radar observations (Fulton et al. 1998) indicate a general northeast–southwest-oriented zone of 6-day total daytime (Fig. 2a) and nocturnal (Fig. 2b) precipitation consistent with the orientation of the midtropospheric trough and surface fronts. Here, significant total precipitation over the southern and central plains occurs both during the day and at night.

The 3–9 July 2003 period that straddles the end of the Bow-Echo and Mesoscale Convective Vortex Experiment (BAMEX; Davis et al. 2004) is representative of the pattern in Fig. 1b. Here, the stage-4 radar observations evince a north–south-oriented pattern of daytime precipitation located west of 100°W (Fig. 2c) and an east–west-oriented zone of heavier nocturnal precipitation associated with MCSs located over the central plains and the Midwest (Fig. 2d). During this period both the synoptic pattern (Trier et al. 2006) and the distribution of precipitation (Fig. 2d) resemble those found in the multiday latitudinal precipitation corridors (Tuttle and Davis 2006).

Comparison of precipitation time series between the two periods (Fig. 3) averaged over the different subdomains in Fig. 2 shows frequent major precipitation events during both periods. However, the area-averaged precipitation amounts were more consistent from day to day and its nocturnal phase more dominant during the BAMEX period (Fig. 3b) characterized by the synoptic pattern in Fig. 1b.

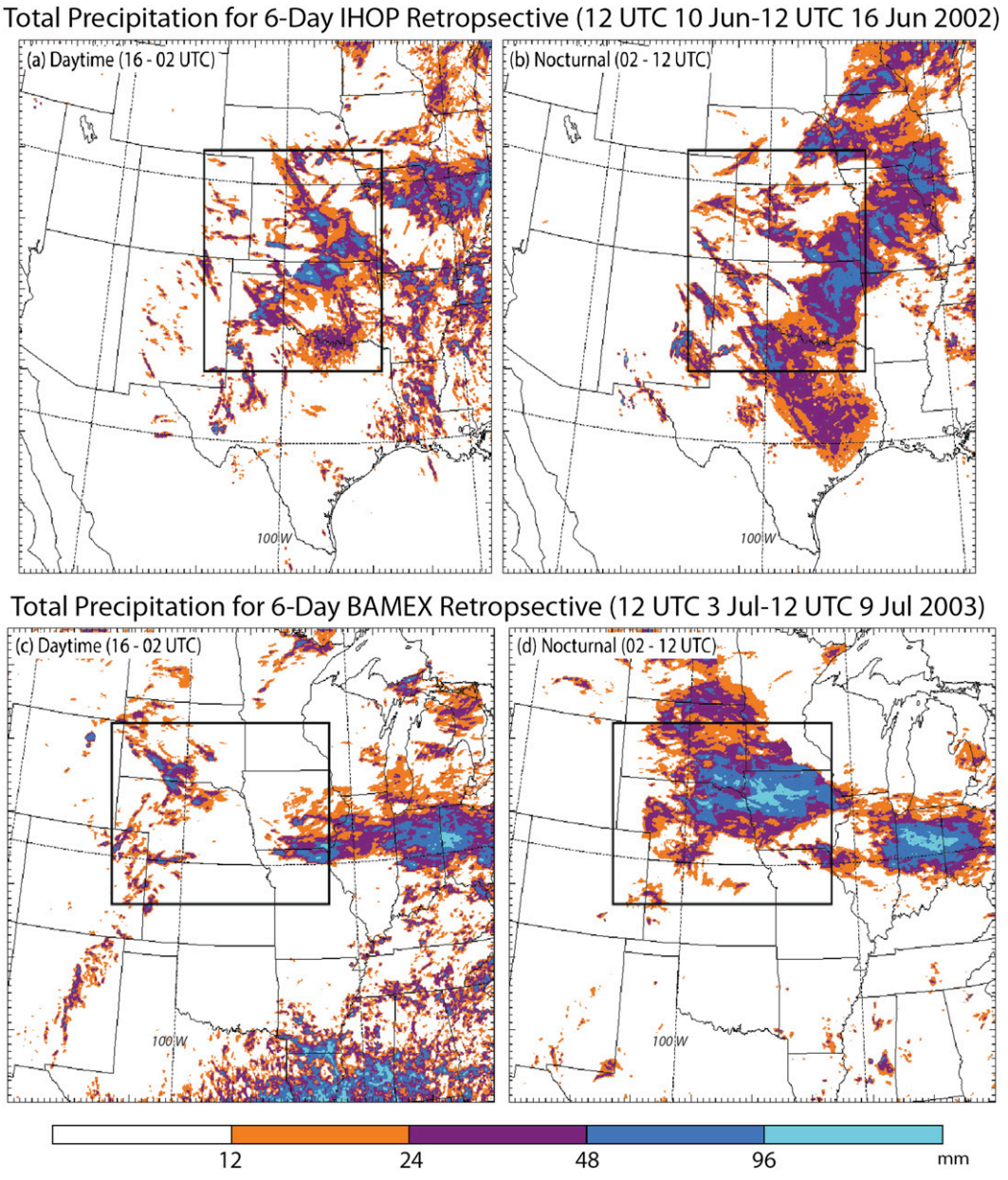

FIG. 2. Total observed (stage 4) precipitation during the 6-day periods that comprise the 0–24-h forecasts discussed in the paper subdivided into (a),(c) 10-h daytime and (b),(d) 10-h nocturnal time intervals. The rectangles indicate the (top) IHOP and (bottom) BAMEX regions of area-averaged time series presented in Fig. 3.

3. Comparison of general characteristics of simulated precipitation with observations

a. Numerical model and experiment design

For each of the two periods we examine six successive 24-h simulations that use the Advanced Research core of the Weather Research and Forecasting Model (ARW-WRF; Skamarock and Klemp 2008) coupled to the Noah land surface model (Ek et al. 2003). For each forecast, the model is initialized at 1200 UTC and contains the same physical parameterizations as those discussed in Part I, which are summarized for convenience in Table 1. As stated in Part I, the simulations from the two different periods occur in different single horizontal domains (Fig. 4) and utilize identical horizontal grid spacing of $\Delta = 3$ km but initial conditions and lateral boundary conditions from different operational modeling systems (Table 2).

The reasons for these differences among the simulations within the different periods are both historical and

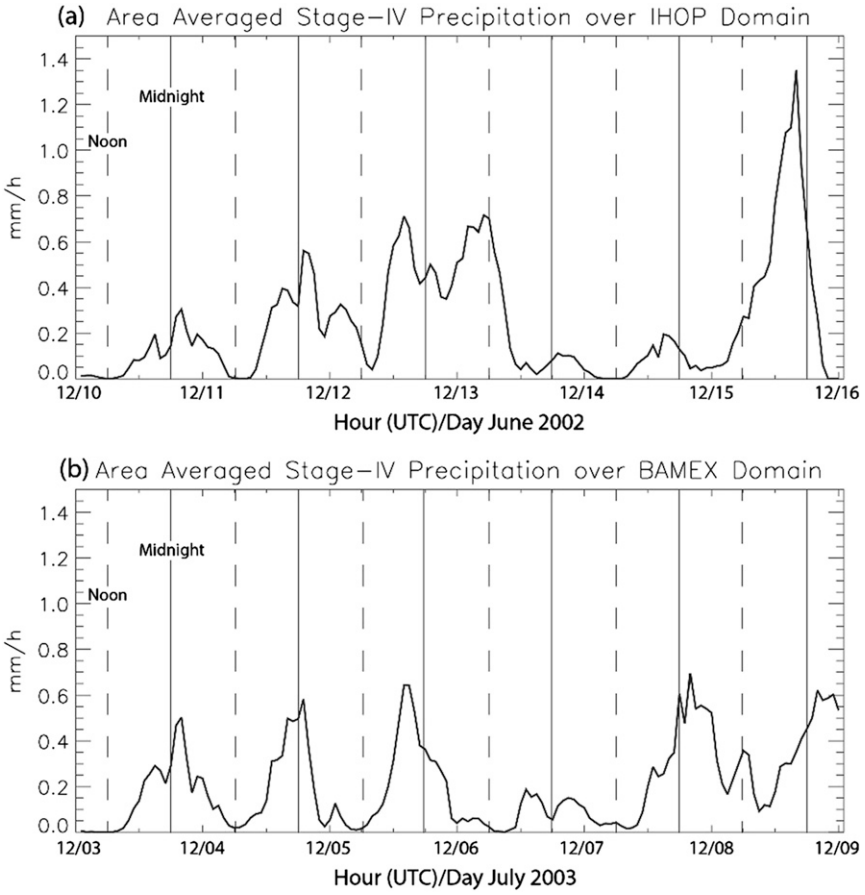

FIG. 3. Time series of hourly precipitation rate derived from stage-4 radar observations for the (a) IHOP and (b) BAMEX 6-day retrospective periods area averaged over the rectangular regions in Figs. 2a,b and 2c,d, respectively. The vertical lines indicate different phases of the diurnal cycle, including approximate local noon (dashed) and midnight (solid). Local daylight time (LT) = UTC − 5 to 6 h.

pragmatic. Since convection during the IHOP period typically began during the afternoon (Fig. 2a), these simulations were first used to study the effects of surface–atmosphere exchanges on CI (Trier et al. 2011a). The BAMEX period was first examined by Trier et al. (2006) to study both MCS propagation and the effects of synoptic and mesoscale forcing on the diurnal cycle of nocturnal convection in a continuously running 6-day simulation with slightly coarser horizontal and vertical grid spacing. In the current study, we have an identical focus for both periods on the examination of physical factors influencing $B_{\min}$, which differs from the previous applications. However, during the course of this research, we found that the more recent 0–24-h simulations for the BAMEX period were better in accommodating the nocturnal precipitation corridor (Fig. 2d) when the domain center was shifted northeastward from that in the IHOP simulations (Fig. 4). For the BAMEX simulations, we also used higher-resolution initial conditions and more frequent boundary conditions from RUC model analyses (Benjamin et al. 2004), instead of the 3-h Environmental Data Assimilation System (EDAS) analyses used for the IHOP simulations. This change resulted

TABLE 1. Physical parameterizations used in each of the twelve 24-h simulations.

Physical parameterization	Scheme (reference)
Longwave radiation	Rapid Radiative Transfer Model (RRTM; Mlawer et al. 1997)
Shortwave radiation	Dudhia (1989)
Planetary boundary layer	Mellor–Yamada–Janjić (Janjić 2002)
Surface layer	Monin–Obukhov similarity (Chen et al. 1997)
Land surface	Noah land surface model (Ek et al. 2003)
Microphysics	Thompson et al. (2008)
Cumulus	None

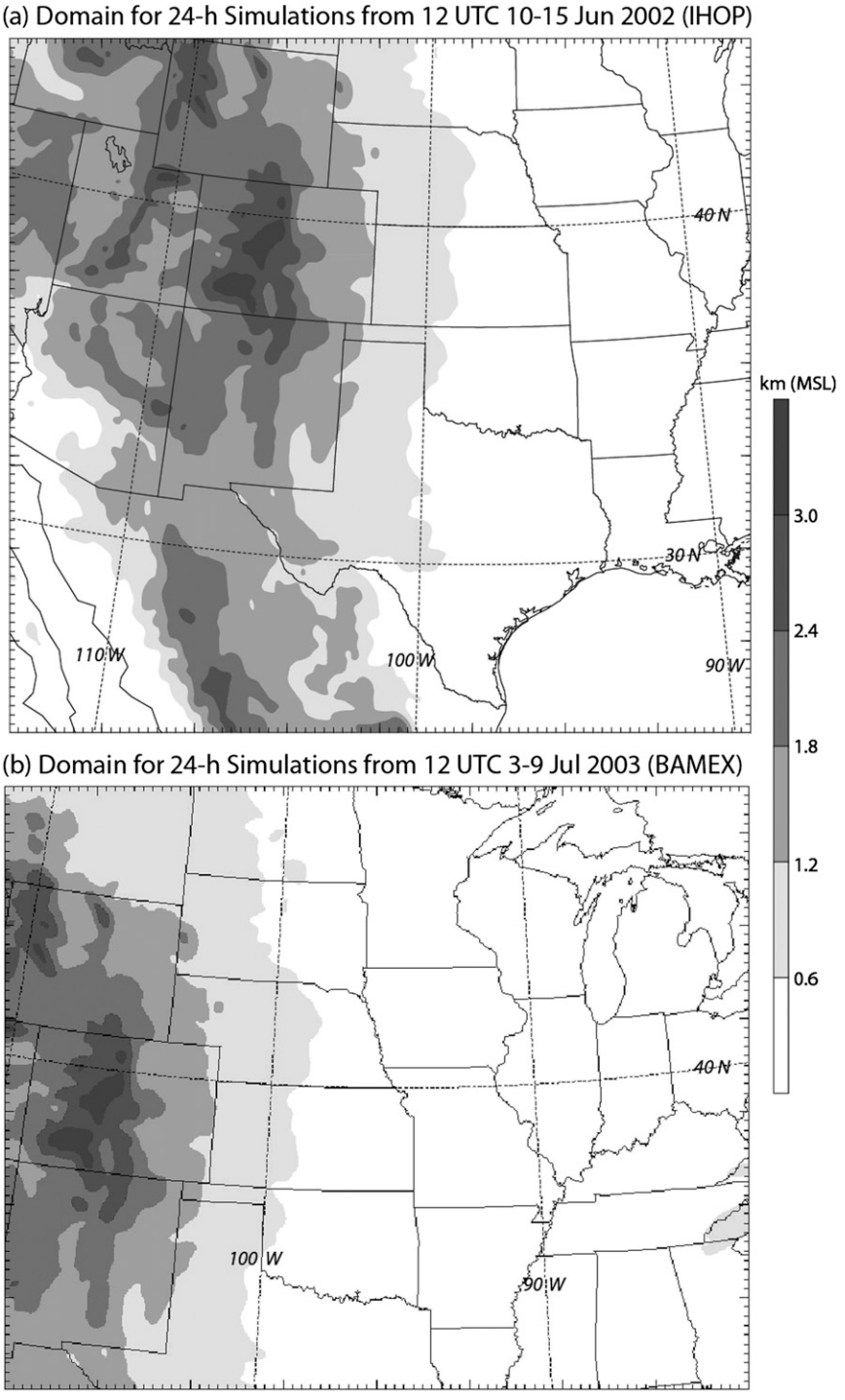

FIG. 4. Domains used for WRF 24-h simulations beginning at 1200 UTC for the 6-day (a) IHOP and (b) BAMEX retrospective periods. The shading indicates the surface elevation in intervals of 0.6 km smoothed to highlight major terrain features.

in further improvements to two of the BAMEX simulations (1200 UTC 4 and 5 July initializations), where the effects of changing the initial and lateral boundary conditions were assessed (not shown). Though the foregoing differences in simulation design could complicate direct comparisons between the simulated IHOP and BAMEX periods, we remind readers that by including simulations from these two different periods our

TABLE 2. Model grid structure, initialization, and forcing for the twelve 24-h simulations during the 10–15 Jun 2002 (IHOP) and the 3–9 Jul 2003 (BAMEX) periods.

Model aspect	10–15 Jun 2002 24-h forecasts from 1200 UTC	3–9 Jul 2003 24-h forecasts from 1200 UTC
Grid points	$800 \times 750 \times 42$	$800 \times 650 \times 43$
Model top	50 hPa	50 hPa
Domain center	35.2°N, 101.6°W	40.0°N, 96.0°W
Atmosphere initial conditions	EDAS analysis $\Delta x = 40$ km	RUC analysis $\Delta x = 20$ km
Land initial conditions	HRLDAS (Chen et al. 2007) $\Delta x = 3$ km	HRLDAS (Chen et al. 2007) $\Delta x = 3$ km
Lateral boundary conditions	EDAS analysis $\Delta t = 3$ h	RUC analysis $\Delta t = 1$ h

intention is simply to add a diversity of different meteorological environments (section 2) to the relatively small sample of simulated MCSs.

b. Precipitation verification

With the exception of some differences to be noted, the overall diurnally averaged simulated hourly precipitation rates area averaged over the IHOP (Figs. 2a,b) and BAMEX (Figs. 2c,d) regions compare well with the identically constructed averages of stage-4 precipitation interpolated onto the model grids (Figs. 5a,c). The cold start in the IHOP simulations may have influenced the more rapid than observed onset of heavy afternoon precipitation (Fig. 5a) since the stabilizing effects of decaying nocturnal convection were not accommodated. However, the late-evening peak is only about 1 h earlier than observed with a similar slow decrease overnight (Fig. 5a). Because of the relatively small amounts of actual observed morning and afternoon precipitation during the BAMEX period, the model cold start may have less influence on the evening onset of heavy precipitation (Fig. 5c). However, the peak in simulated

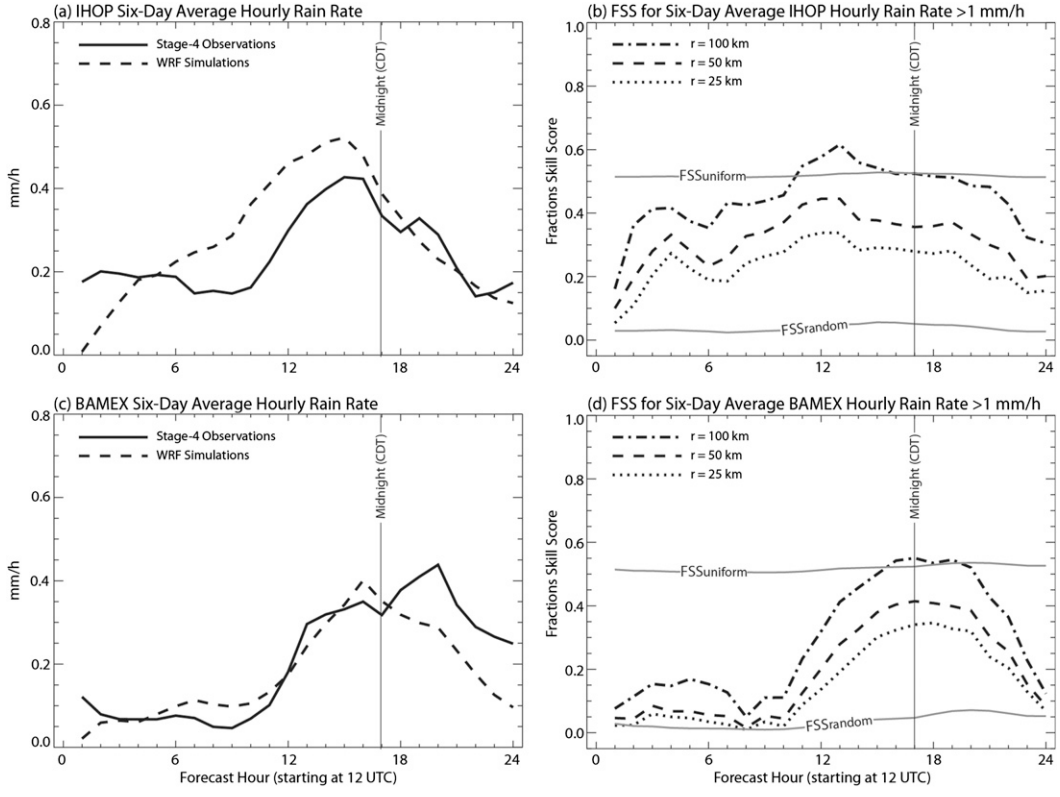

FIG. 5. Comparison of the 6-day diurnally averaged hourly precipitation rate from stage-4 radar observations and 0–24-h simulations beginning at 1200 UTC for the (a) 10–15 Jun 2002 IHOP and (c) 3–9 Jul BAMEX periods area averaged over the rectangular regions in Figs. 3a,b and 3c,d, respectively. Corresponding diurnally averaged FSSs of rain rate exceeding 1 mm h^{-1} for different radii of influence for the 6-day (b) IHOP and (d) BAMEX periods. The FSS curves for random forecast skill (FSS_{random}) and halfway ($FSS_{uniform}$) between random and perfect forecast skill (see text for discussion) are shown for reference.

precipitation during BAMEX around local midnight is about 3 h earlier than observed (Fig. 5c).

Diurnally averaged fractions skill scores (FSSs) indicate the horizontal scales at which forecasts are skillful (e.g., Roberts and Lean 2008; Schwartz et al. 2009) for the aggregates of six IHOP and BAMEX simulations in Figs. 5b and 5d, respectively. Improvement over random skill for forecasts of precipitation intensities >1 mm h^{-1} is evident for all three chosen radii of influence (r = 25, 50, and 100 km) at nearly all times. According to Roberts and Lean (2008), acceptable forecast skill occurs if FSS $\geq$ FSS$_{\text{uniform}}$, where FSS$_{\text{uniform}} = 0.5 + f_o/2$ and f_o = FSS$_{\text{random}}$. Thus, we conclude that reasonable skill occurs at scales $\geq$100 km (Figs. 5b,d) during the heaviest area-averaged rainfalls (cf. Figs. 5a,c) near average MCS maturity times.

4. Methods of case selection and compositing of mature MCS environments

a. Selection of MCSs

Simulated MCSs used in the composites are required to persist for at least 3 h and have either contiguous or adjacent clusters of model-derived reflectivity $\geq$40 dBZ over horizontal scales of 200 km or more. The mature stages of MCSs (Fig. 6) are defined by the times at which the areal coverage of model-derived reflectivity $\geq$40 dBZ is maximized. This typically occurs 2–3 h after the maximum local intensity of convection within the MCSs and closer to the times of maximum area-averaged precipitation (e.g., Figs. 3 and 5a,c). These results are broadly consistent with results based on other definitions of MCS life cycles (e.g., Maddox et al. 1986; McAnelly and Cotton 1989).

Only simulated MCS cases that had an observational analog within ~3 h and ~200 km were included for analysis of their mature environments. These criteria resulted in a large majority (~80%) of simulated MCSs that met the above structural requirements being selected, which is consistent with the forecast skill defined by the FSSs for r = 100 km (Figs. 5b,d) during the late evening and overnight when MCSs mature.

b. Defining the MCS environment

The MCS-relative inflow is calculated at the mean level of maximum equivalent potential temperature θ_e located within 40–90 km of the MCS leading edge, which itself is defined by the 25-dBZ model-derived reflectivity contour. The MCS leading-edge position is linearly interpolated for cases that contain gaps where this reflectivity is not exceeded. The MCS translation speed is defined by the 2-h displacement of its leading edge centered on the time of its maturity. The MCS environment is defined as the region located up to 250 km outward from the leading edge and is oriented along the MCS-relative inflow, as shown in Fig. 7a.

For comparison purposes we choose the width (i.e., dimension in the cross-inflow direction) of the MCS environment to be that approximated by the leading-edge scale of the smallest MCSs.[1] Clearly, this is only a fraction of the leading-edge scale of the larger MCSs (Fig. 6). For the larger MCSs we select as their environments regions upstream from the most intense convection or regions toward the center of their leading edge when the intensity of the convection appears more uniform (Fig. 6).

For some of the larger MCSs multiple environments are defined. This occurs for MCSs with either 1) multiple convective features oriented at significantly different angles (Fig. 6h) or 2) significant thermodynamic variations along their leading edge (Fig. 6n). A total of 22 environments were defined for the 20 selected MCSs (Fig. 6).

Variations of different quantities with upstream distances from the MCS leading edge are discussed in the remainder of the paper. To assess such variations, the minimum distance from the interpolated MCS leading edge was calculated for each horizontal grid point within the zone bounded by the leading edge and the sides of the environment region defined by the MCS-relative inflow orientation (Fig. 7a). Values of quantities at these grid points are then averaged within twenty-five 10-km-wide bins whose centers range in distance between $\bar{r}$ = 5 and 245 km from the MCS leading edge. To mitigate possible contamination of these averaged quantities by condensation effects ahead of the MCS, all grid points with maximum column reflectivities $\geq$25 dBZ are excluded.

c. MCS environment categories for composites

The average time of the mature stage of the 20 simulated MCSs selected is 0430 UTC [2330 local time (LT), which is UTC − 5 h]. The sizeable temporal lag in maximum climatological thunderstorms (e.g., Wallace 1975) and precipitation frequency (e.g., Carbone et al. 2002) from the cessation of significant daytime heating is well known for the central and southern plains region. The maturation of the MCSs at night has implications

[1] Due to the requirement that the MCS environment had to be simultaneously oriented along the storm-relative inflow and associating it with the specific leading-edge geometry in individual cases, the widths of the selected MCS environments are similar but not identical.

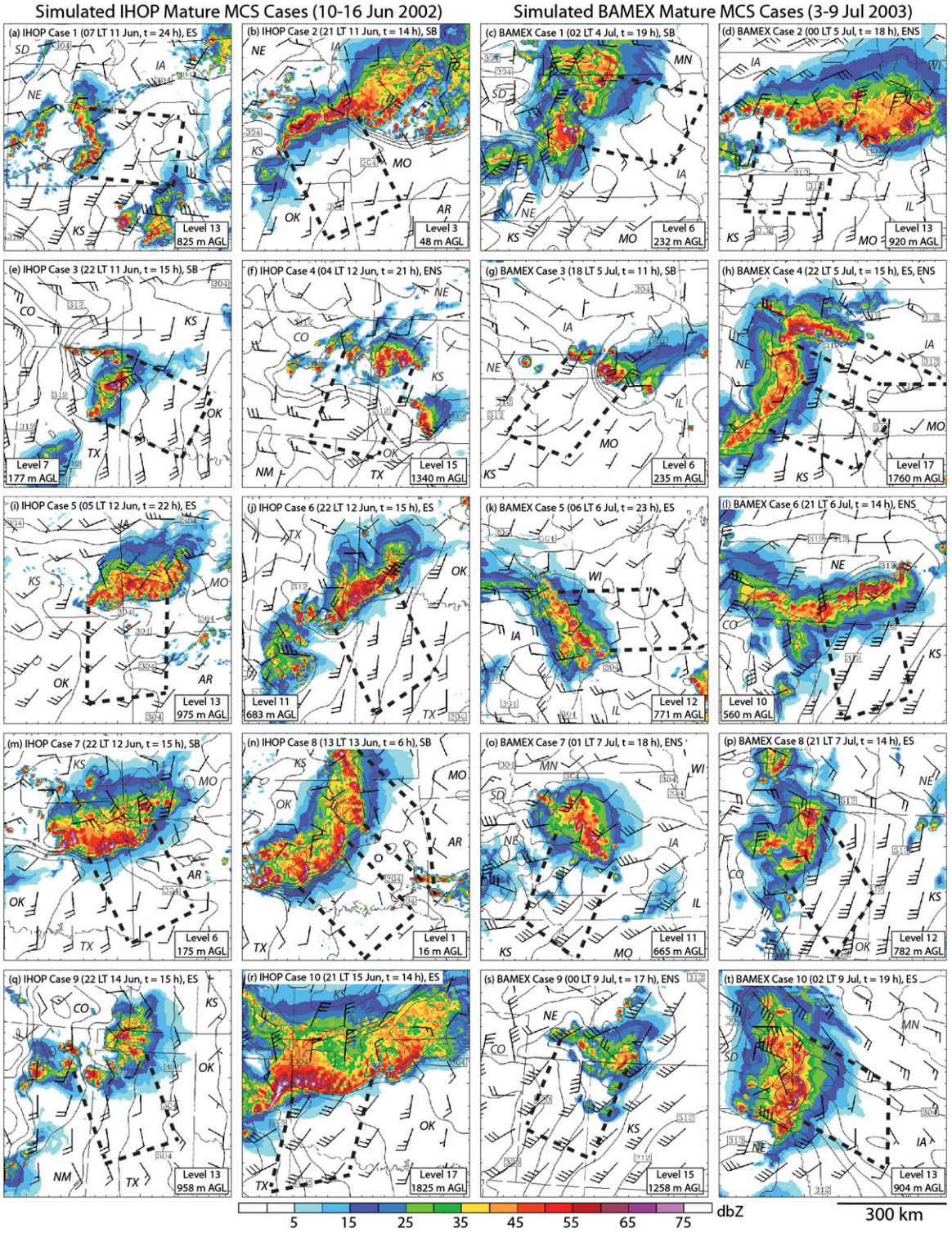

FIG. 6. Simulated mature MCS cases from the 6-day (left two columns) IHOP and (right two columns) BAMEX retrospective periods used in the composite analysis. Each panel has the vertical column maximum model-derived reflectivity (color scale) and the ground-relative winds and potential temperature (2.5-K contour intervals) at the indicated model levels chosen where equivalent potential temperature is maximized within the dashed regions defining the MCS environment near the leading edge of the model-derived reflectivity. The composite MCS categories are indicated as follows: SB, surface based; ES, elevated squall; and ENS, elevated nonsquall (see text for further discussion).

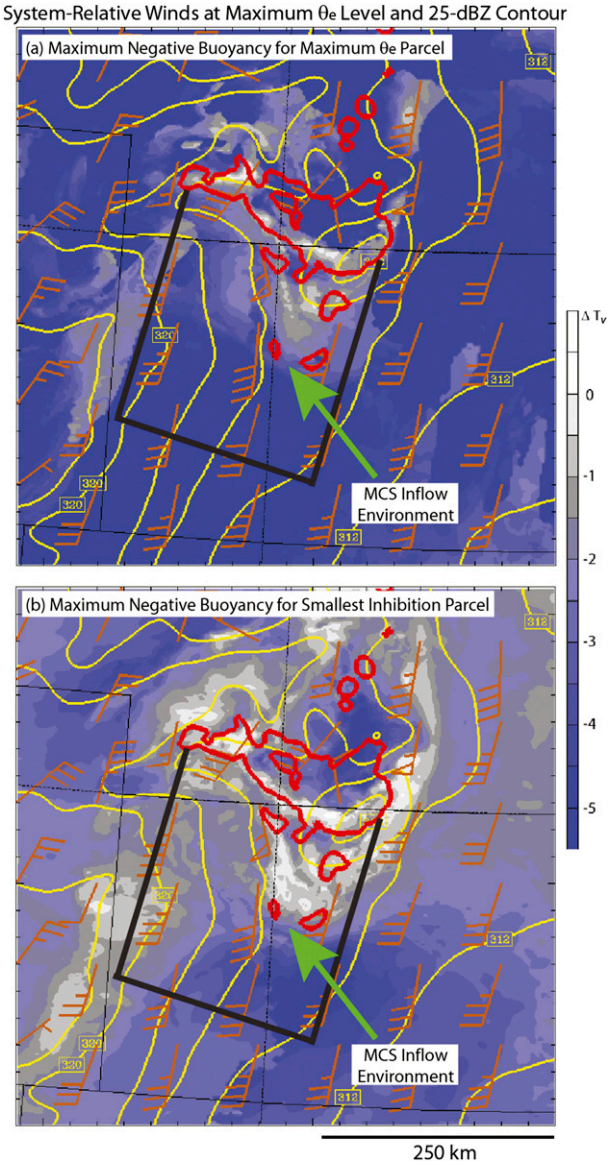

FIG. 7. Example (from BAMEX case 9; Fig. 6s) illustrating the mature MCS environment defined by the region bounded by the black lines and the edge of the 25-dBZ model-derived reflectivity contour (red), at which the MCS-relative flow (tan wind barbs) is oriented along an approximate inward normal direction. The yellow contours indicate potential temperature and the minimum parcel buoyancy ($B_{\min}$) is shown by colored shading for air parcels originating at (a) the level of maximum equivalent potential temperature in the vertical column and (b) the parcel origination level in the vertical column for which $B_{\min}$ is maximized (i.e., is least negative).

for whether their convection is driven by environmental air parcels remaining in contact with the surface or by air parcels originating from significantly above the surface, where the air is less exposed to radiative cooling and thermodynamic stabilization. Moreover, these elevated parcels may be associated with destabilizing advection associated with the nocturnal LLJ.

Motivated by the desire for a physically based classification of MCS type (as in Fritsch and Forbes 2001), we first divide the MCS environments into ones supporting surface-based (SB) or elevated (E) convection. In reality, some nocturnal convective environments support both types of convection simultaneously (e.g., Trier et al. 2011b). For an MCS to be classified as surface based, we require both 1) air parcels with highest θ_e in the vertical column be located below 0.5 km AGL and 2) that the largest (i.e., least negative) $B_{\min}$ of all air parcels in the vertical column with significant CAPE $\geq$ 250 J kg^{-1} be located below 1 km AGL when averaged from 40 to 90 km of the MCS inflow edge. The second criterion reflects our finding that the highest θ_e (often referred to as the most unstable) air parcel in a vertical column does not generally possess the smallest $B_{\min}$ magnitude, as can be seen by a comparison of Figs. 7a and 7b. Together the two criteria help ensure that environments with elevated parcels that have significant CAPE with small convective inhibition are not excluded from the elevated class. However, it does not preclude the possibility that surface-based convection could also occur.

Applying the above criteria yields 7 surface-based and 15 elevated MCS environments (Table 3). We further subdivide the elevated MCS environments into squall (ES) and nonsquall (ENS) categories. For an MCS to be considered a squall, it must have a component of its movement exceed 9 m s^{-1} along the outward normal vector of its mean leading-edge orientation. This aspect of our classification has similarities to the Barnes and Sieckman (1984) classification of ''fast moving'' and ''slow moving'' tropical convective lines, and is expected to place MCSs whose overall propagation is significantly influenced by their cold pools in the ES category.

Striking differences in this component of system motion among the seven ENS and nine ES environments are evident in Table 3, which indicates that the ES MCSs move almost perpendicular to their orientation and that the smaller overall motion in ENS MCSs is approximately parallel to their orientation. The MCS category (SB, ENS, or ES) is provided in Fig. 6 along with the model-derived maximum reflectivity in the column and ground-relative winds and potential temperature at the model level at which average θ_e is maximized for r = 40–90 km from its leading edge. Note that all ENS MCSs are either aligned along east–west-oriented fronts [Figs. 6d, 6f, 6h (north environment), and 6l] or are located in other areas of prominent warm advection (Figs. 6o,s). The ES cases, which like the ENS cases, reach their mature stage from midevening to the early morning

TABLE 3. Time of maturity, MCS speed, and component of MCS speed along the vector oriented outward normal from the MCS leading edge for simulated cases falling within the three composite categories of MCS type, including ENS, ES, and SB MCSs. Maximum model-derived reflectivity and environmental conditions at the time of MCS maturity (see text) are displayed in Fig. 6 for the case identifications provided in the left column. Boldface font indicates the category averages.

MCS case	Mature time (UTC)	MCS speed ($m\,s^{-1}$)	Normal component ($m\,s^{-1}$)
IHOP 4	0900 (0400 LT)	5.0	1.2
BAMEX 2	0500 (0000 LT)	10.0	−1.4
BAMEX 4 (NE band)	0300 (2200 LT)	18.8	−6.9
BAMEX 6	0200 (2100 LT)	8.5	2.7
BAMEX 7	0600 (0100 LT)	14.8	−8.8
BAMEX 9	0500 (0000 LT)	9.5	−1.9
ENS avg (six cases)	**0500 (0000 LT)**	**11.1**	**−2.5**
IHOP 1	1200 (0700 LT)	21.8	21.8
IHOP 5	1000 (0500 LT)	12.5	11.0
IHOP 6	0300 (2200 LT)	12.7	12.5
IHOP 9	0300 (2200 LT)	10.7	10.0
IHOP 10	0200 (2100 LT)	15.2	15.1
BAMEX 4 (SW band)	0300 (2200 LT)	18.8	17.5
BAMEX 5	1100 (0600 LT)	14.0	14.0
BAMEX 8	0200 (2100 LT)	14.8	14.3
BAMEX 10	0700 (0200 LT)	22.4	22.4
ES avg (nine cases)	**0550 (0050 LT)**	**15.9**	**15.4**
IHOP 2	0200 (2100 LT)	10.4	9.6
IHOP 3	0300 (2200 LT)	14.0	11.4
IHOP 7	0300 (2200 LT)	9.9	9.8
IHOP 8 (SW band)	1800 (1300 LT)	13.3	13.2
IHOP 8 (N band)	1800 (1300 LT)	13.3	10.4
BAMEX 1	0700 (0200 LT)	16.9	13.3
BAMEX 3	2300 (1800 LT)	8.5	8.3
SB avg (seven cases)	**0015 (1915 LT)**	**12.3**	**10.9**

hours (Table 3), are typically located in less baroclinic regions. However, a few large ES systems [e.g., Figs. 6t, 6h (south environment)] are located within, and are oriented approximately normal to, surface baroclinic zones as conceptualized by the nearly vertical dashed line in Fig. 1b.

5. Composite environments

a. Horizontal variability of vertical shear and thermodynamic variables

Along with the differences in MCS movement among the ENS and ES cases (Table 3) the 0.5–3.0-km AGL bulk vertical shear normal to the mean MCS orientation is substantially different (Figs. 8a,b). The distribution of vertical shear for ENS MCSs (Fig. 8a) is consistent with a frontal boundary between the far environment ($r >$ 100 km) and the MCS leading edge ($r = 0$ km), where the average MCS-normal vertical shear is negative. The latter finding indicates that MCS maintenance in ENS cases is supported by mechanisms other than those proposed by RKW.

In contrast to the ENS environment, the ES environment has little variation in the MCS-normal vertical shear with distance from the leading edge (Fig. 8b). Though there are large variations in its magnitude among individual cases, the average value of the ES MCS-normal vertical shear in the 0.5–3.0-km AGL layer is $\overline{\Delta U} \sim 10\,m\,s^{-1}$. The SB environments also have 0.5–3.0-km AGL MCS-normal vertical shear that is approximately uniform with distance from the MCS leading edge, but the average magnitude is weaker with $\overline{\Delta U} \sim 5\,m\,s^{-1}$ (Fig. 8c).

In nearly all cases the air parcel with the smallest B_{min} magnitude in the vertical column is located within 40 km from the leading edge and has $B_{min} > -2$ K (Figs. 9a,c,e), which is consistent with small CIN (Part I, their Fig. 8). The ENS (Fig. 9a) and ES (Fig. 9c) MCS environments have a more significant average increase in the magnitude of B_{min} with distance from the leading edge than the SB cases (Fig. 9e) for both the smallest magnitude B_{min} and largest θ_e parcels in the vertical column, whose average heights are given in Figs. 9b,d,f. The significant gradual increase in average B_{min} magnitude with distance from the leading edge over horizontal scales of $r > 100$ km suggests that physical processes in addition to strong localized lifting at a finescale boundary (as proposed in RKW) are influential in favoring the sustenance of deep convection in the elevated cases,

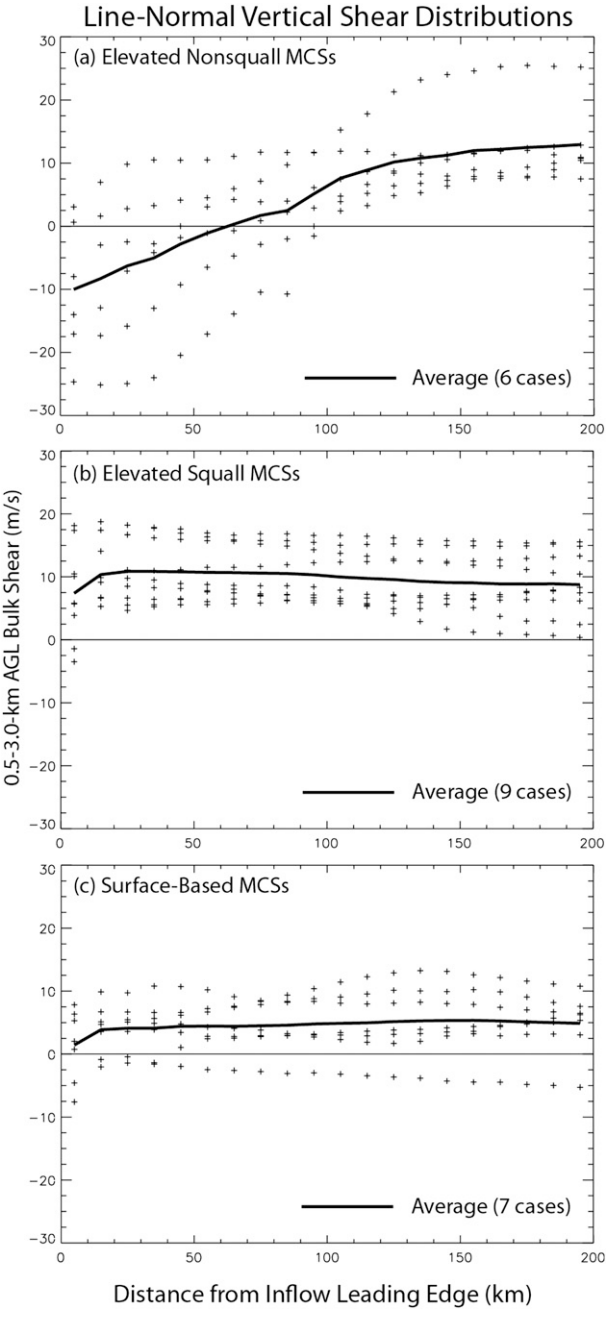

FIG. 8. Distributions of 0.5–3.0-km AGL approximate line-normal vertical shear vs distance from the MCS leading edge averaged along the width between the two parallel dashed lines in Fig. 6 and within 10-km distance bins in the direction normal to the local MCS leading edge for (a) elevated nonsquall, (b) elevated squall, and (c) surface-based MCS environments. In these distributions the approximate line-normal shear direction is defined by the orientation of the black-colored sides of the polygons enclosing the MCS environment and is antiparallel to the system-relative inflow in individual cases such as that shown in Fig. 7.

including MCSs that propagate like squall lines. This is noteworthy considering recent case studies (e.g., Coniglio et al. 2012) and reviews (e.g., Bryan et al. 2012) focusing on the application of RKW theory.

b. Composite vertical structure

In Fig. 10 CAPE and $B_{\min}$ are plotted as a function of parcel origination height AGL, where 50-hPa-deep averaged air parcels centered on different model levels are used in the calculations. The $B_{\min}$ magnitudes decrease significantly toward the MCS leading edge for the composite of all 22 MCS environments, while CAPE magnitudes increase (Fig. 10a). The $B_{\min}$ decreases begin beyond $r = 250$ km (not shown) and are most pronounced within $r = 100$ km (Fig. 10a).

The gradual decrease in $B_{\min}$ magnitude toward the leading edge is a common characteristic among composite categories (Figs. 10b–d). However, the smallest $B_{\min}$ magnitudes in these plots are larger than corresponding values in Fig. 9 (solid curves) because of the variability in altitude of the smallest $B_{\min}$ magnitude among cases within the composite categories.

Though the overall increase in $B_{\min}$ magnitude with distance from the MCS leading edge is similar, there are important differences among these composite environments. The SB MCS composite (Fig. 10b) has the smallest-magnitude $B_{\min}$ and the largest CAPE ($>2000\,\mathrm{J\,kg^{-1}}$), which are approximately collocated near the ground. The ENS composite shows a more distinct vertical separation between the maximum CAPE, which is between 0.5 and 1.0 km, and the smallest magnitudes of $B_{\min}$, which are located between 1.0 and 2.5 km AGL (Fig. 10c). This finding has implications for cumulus parameterizations in coarser-resolution models.

The ES composite (Fig. 10d) is intermediate between the ENS (Fig. 10c) and the SB (Fig. 10b) composites. The propagation characteristics of these MCSs are broadly similar to the SB category (Table 3), as most of the SB MCSs also behave as squalls. However, the average time of maturity of the ES MCSs within the diurnal cycle, at or slightly after local midnight, is similar to the ENS cases (Table 3).

With gradual decreases in magnitude of $B_{\min}$ toward the MCS leading edge being a robust feature of the environmental composite for all MCSs (Fig. 10a) that has implications for the sustenance of the MCSs, we now examine physical processes that could account for this. Local 3-h increases in $B_{\min}$ (i.e., reductions in the negative buoyancy) preceding MCS maturity extend outward for approximately 100 km from the MCS leading edge in the composite for all cases (Fig. 11a). The horizontal variability of these 3-h $B_{\min}$ changes (Fig. 11a) within the region ~100 km from the MCS leading edge

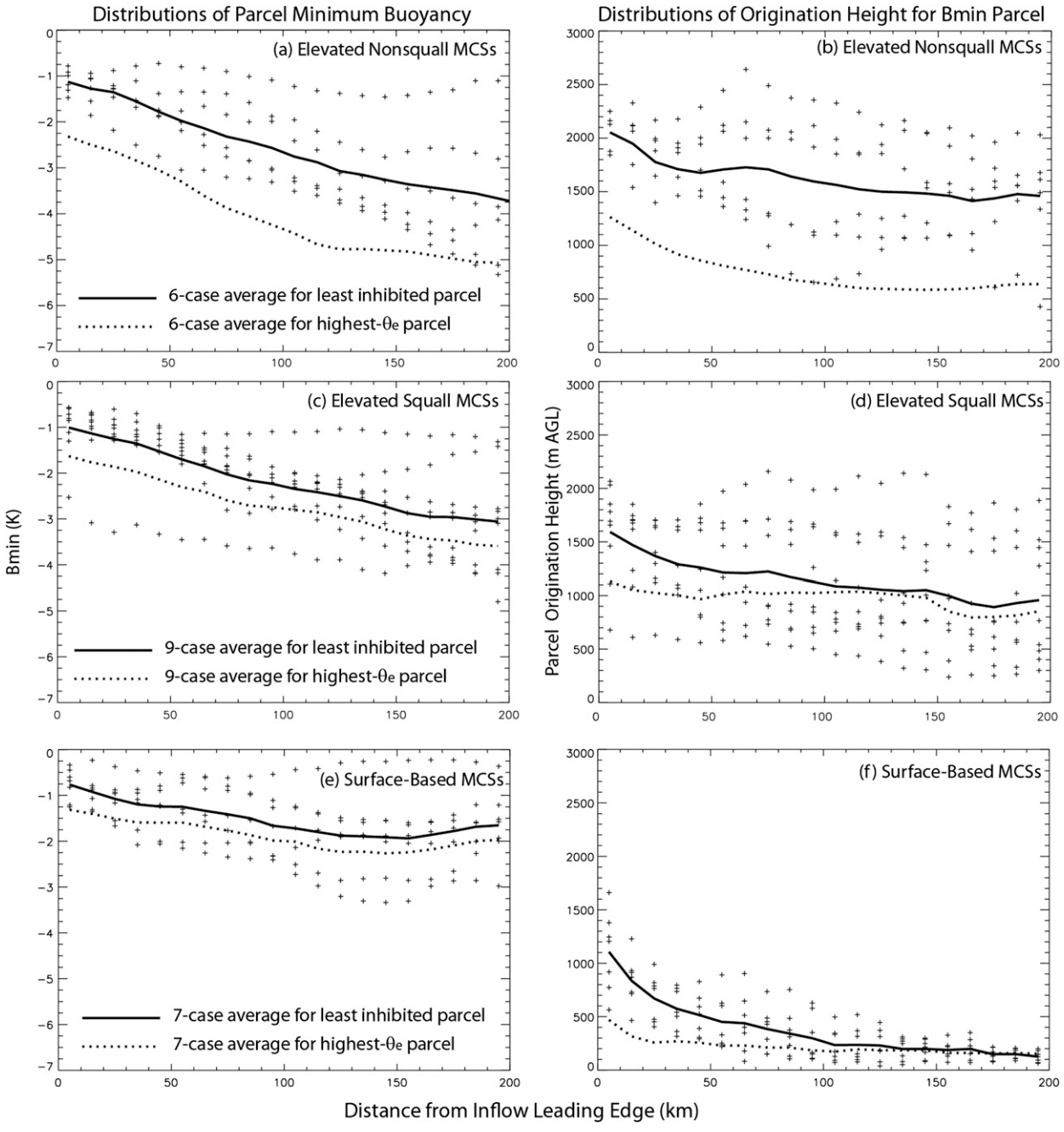

FIG. 9. (left) Distributions of $B_{\min}$ averaged along the width between the two parallel dashed lines in Fig. 6 and within 10-km-distance bins oriented normal to the local MCS leading edge for air parcels originating at the level for which $B_{\min}$ is maximized (is the least negative) for the (a) elevated nonsquall MCSs, (c) elevated squall MCSs, and (e) surface-based MCSs. (right) Identically averaged distributions of the origination height AGL of the maximum $B_{\min}$ parcels plotted on the left for the (b) elevated nonsquall MCSs, (d) elevated squall MCSs, and (f) surface-based MCSs. The solid line in each panel is the average of the distribution in each plot and the dotted lines are averages for air parcels originating at the height of maximum equivalent potential temperature (distributions not shown).

has the same sign as the instantaneous horizontal gradients of $B_{\min}$ at the end of the period (Fig. 10a), indicating that, overall, recent local events contribute to the gradual decreases in $B_{\min}$ magnitude as one moves toward the MCS from within approximately $r < 100$ km.

However, as for the instantaneous $B_{\min}$ in Fig. 10, there are important differences among individual composites (Figs. 11b–d). The most widespread temporal decreases in negative buoyancy occur in the SB composite (Fig. 11b). This is not surprising considering the

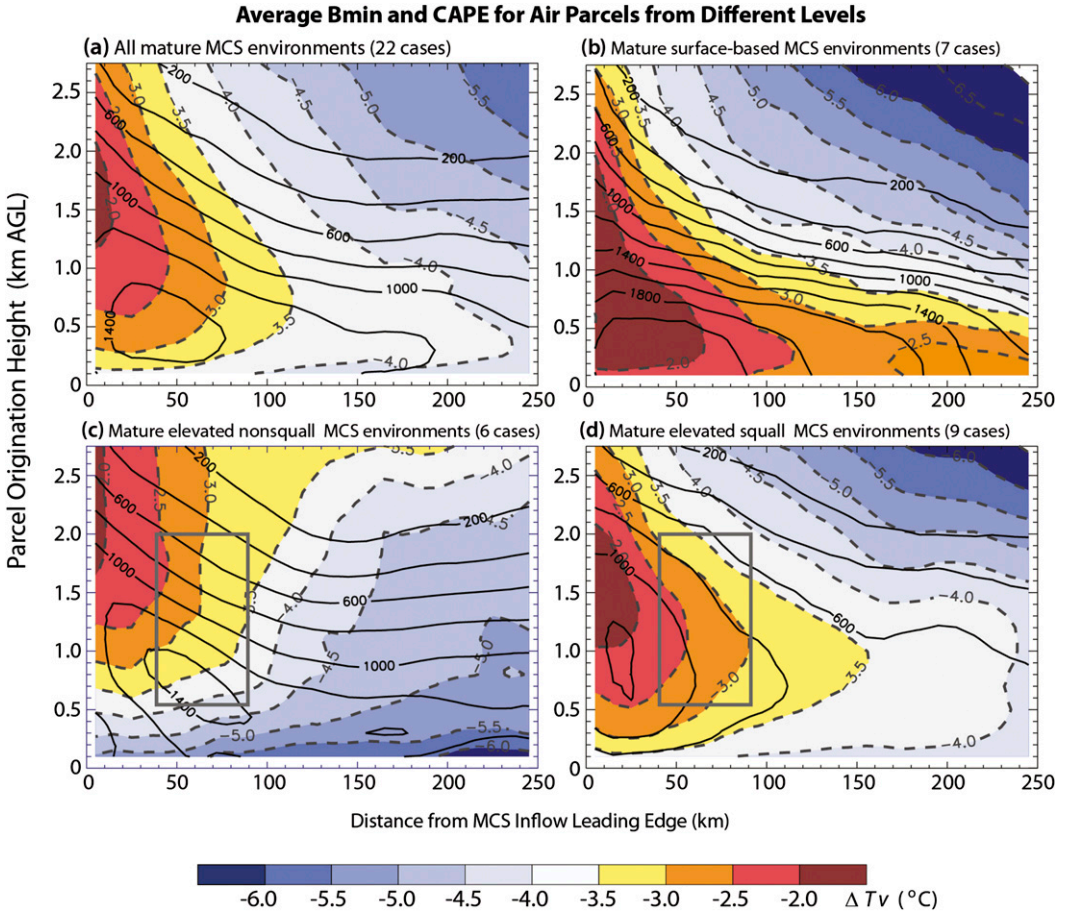

FIG. 10. Average buoyancy minimum B_{min} expressed in virtual temperature ΔT_v units (color scale and red dashed contours with 0.5°C intervals) and CAPE (black contours with 200 J kg^{-1} intervals) for air parcels originating at the indicated levels averaged along the width between the two parallel dashed lines in Fig. 6 and within 10-km-distance bins in the direction normal to the local MCS leading edge for environments of (a) all mature MCSs, (b) surface-based MCSs, (c) elevated nonsquall MCSs, and (d) elevated squall MCSs. The rectangular regions in (c) and (d) indicate the locations over which the B_{min} budget calculations presented in Figs. 15–17 are performed.

earlier average occurrence in the diurnal cycle of the mature stage for these MCSs. The effects of daytime heating occurring in several of these MCS environments (e.g., Figs. 6g,n) contribute to at least some B_{min} increase over widespread areas near the ground (Fig. 11b). The enhancement of these increases near the MCS leading edge (Fig. 11b), which also occurs in the other composite categories (Figs. 11c,d), is related to other factors.

Greater temporal increases in B_{min} (reductions in negative buoyancy) and in their horizontal gradients above the surface occur for the ES composite (Fig. 11d) than for the ENS composite (Fig. 11c). The relatively modest temporal changes in the ENS composite (Fig. 11c) may partly reflect the slower MCS movement than for the ES composite. The slower movement of ENS MCSs indicates that convection has been supported near or within this environment during the 3-h period during which the B_{min} changes are calculated. Continued local destabilization may thus be less necessary for MCS sustenance than in the environment of mature propagating ES MCSs (Table 3), which did not support convection in the same location 3 h earlier.

The small temporal B_{min} changes during the 3 h preceding the mature stage of ENS MCSs occur despite warm advection (Fig. 12c) that is considerably stronger than for the composite comprising all 22 MCS environments (Fig. 12a) and the composite environments of the ES and SB MCS categories (Figs. 12b,d). Mesoscale ascent, which occurs in all composites (Fig. 13), is commonly associated with environments of warm advection and is by far the strongest in the ENS environment (Fig. 13c).

Thus, the relatively small B_{min} changes for the ENS environment appear related to strong cancellation among

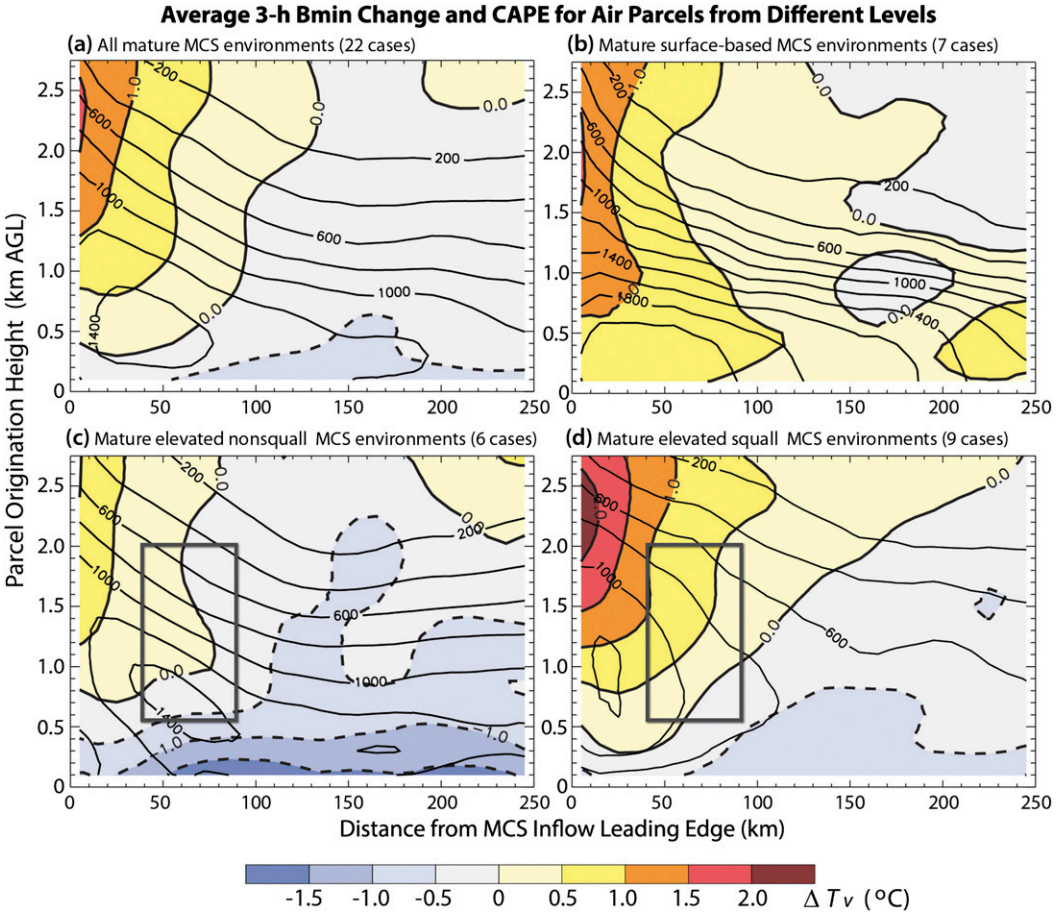

FIG. 11. As in Fig. 10, but with the color shading indicating the average 3-h change in B_{min} ending at the time of MCS maturity for air parcels originating at the indicated levels.

different environmental forcings, which is exemplified in Fig. 12c. Another factor to be kept in mind is that B_{min} is influenced not only by environmental changes at air parcel origination levels but also by changes at levels above, where the parcels attain their values of minimum buoyancy. Because of this, temporal B_{min} changes can be quite sensitive to vertical variations in horizontal temperature advections and vertical motions. In the next section we use budget calculations to quantify these effects of environmental forcing on B_{min} changes.

6. Budget calculations

a. Budget methodology

In this section we analyze and contrast the composites of only the elevated MCS (ENS and ES) environments. This choice avoids the complication of mixing cases with maturation times ranging from midday to overnight in a small composite. In the SB composite there are both afternoon cases where surface fluxes of heat and moisture strongly influence B_{min} evolution and other cases, which despite being surface based, may have more in common with ES cases. The ability for preexisting organized convection to remain surface-based even after substantial nocturnal surface cooling occurs has been demonstrated in idealized simulations (Parker 2008).

The B_{min} budgets for the ENS and ES composites are calculated for air parcels whose origination levels are from 0.5 to 2 km AGL. These levels are deemed most important because they encompass the intersection between altitudes whose air parcels have significant CAPE and B_{min} magnitudes (within 100 km of the MCS leading edge) that are not prohibitively large for supporting convection (Figs. 10c,d).

Since the convection in these composites of mature MCS cases occurs after sunset (Table 3) and is elevated, we concentrate on the influence of grid resolved-forcing terms on buoyancy changes (GRES) and make no attempt to account for influences of surface fluxes, which at these times are small. Another diabatic effect that we neglect is the radiative temperature change, which is

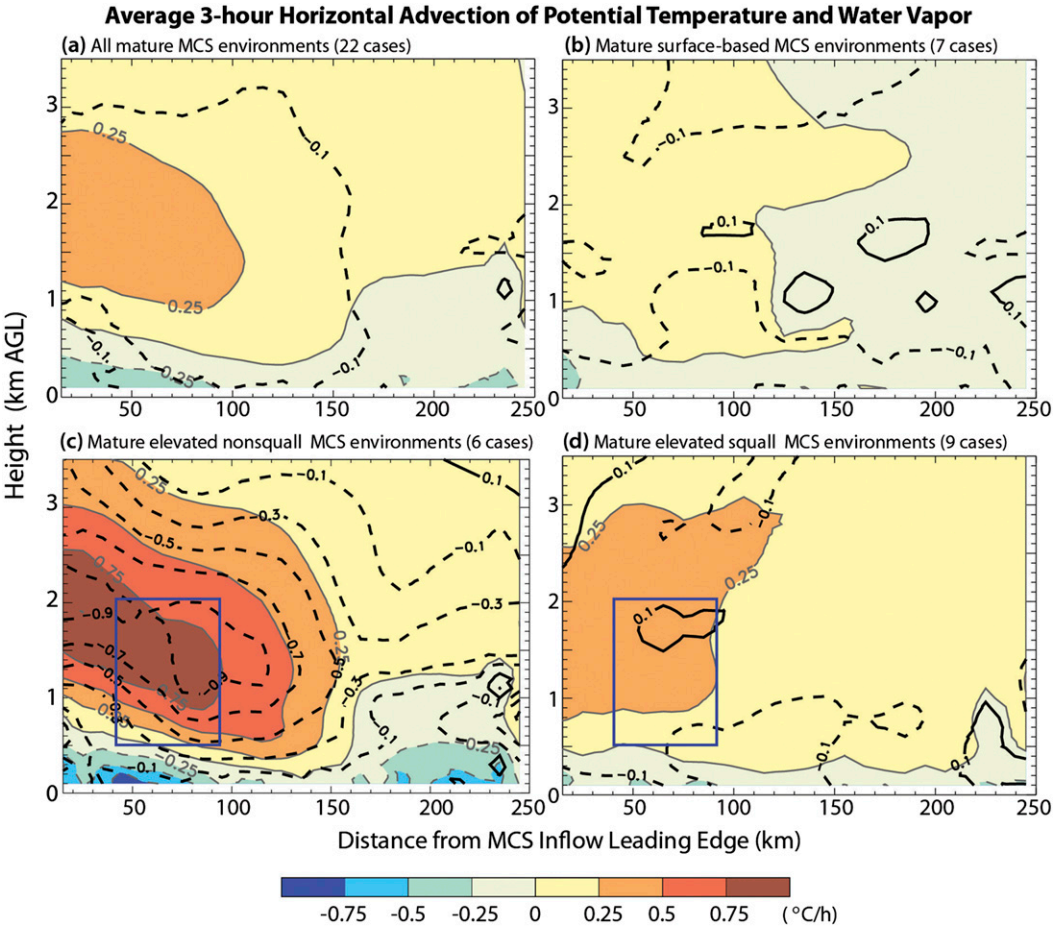

FIG. 12. Average horizontal vapor mixing ratio advection (black contours with 0.2 g kg^{-1} h^{-1} contour intervals, zero contour omitted and negative values dashed) and horizontal temperature advection (color shading with 0.25°C h^{-1} contour intervals) averaged along the width between the two parallel dashed lines in Fig. 6 and within 10-km-distance bins in the direction normal to the local MCS leading edge for environments of (a) all mature MCSs, (b) surface-based MCSs, (c) elevated nonsquall MCSs, and (d) elevated squall MCSs. The rectangular regions in (c) and (d) indicate the locations over which the $B_{\min}$ budget calculations presented in Figs. 15–17 are performed.

likely significant in the lowest few hundred meters due to nocturnal surface cooling, but is unlikely to have a strong impact on $B_{\min}$ for elevated parcels. Apart from the neglect of surface fluxes, we use the methodology detailed in section 4 of Part I. Here, the 3-h time-averaged virtual temperature (buoyancy) change from grid-resolved forcing, GRES = $\delta T_{\mathrm{vp}} - \delta T_{\mathrm{ve}}$, is compared to the actual simulated 3-h virtual temperature (buoyancy) change, ΔBUOY, at the level of the lifted parcels p_B. As in Part I, p_B is held constant during the 3-h period for each parcel origination level at individual horizontal grid points, and is the average pressure at which $B_{\min}$ occurs for parcels originating at these locations during the 3-h period.

The part of GRES due to the forcing for the changes to the parcel at its origination level,

$$\delta T_{\mathrm{vp}}|_{p_B} = \mathrm{HTADV}_P + \mathrm{VTADV}_P + \mathrm{HMADV}_P + \mathrm{VMADV}_P, \quad (1)$$

which are manifested at its lifted level p_B, has contributions due to horizontal temperature advection [first term on the right side of (1)], a combination of adiabatic temperature change and vertical temperature advection [second term on the right side of (1)], horizontal moisture advection [third term on the right side of (1)], and vertical moisture advection [fourth term on the right side of (1)]. Analogously, the part of GRES due to the forcing for environmental changes,

$$-\delta T_{\mathrm{ve}}|_{p_B} = \mathrm{HTADV}_E + \mathrm{VTADV}_E, \quad (2)$$

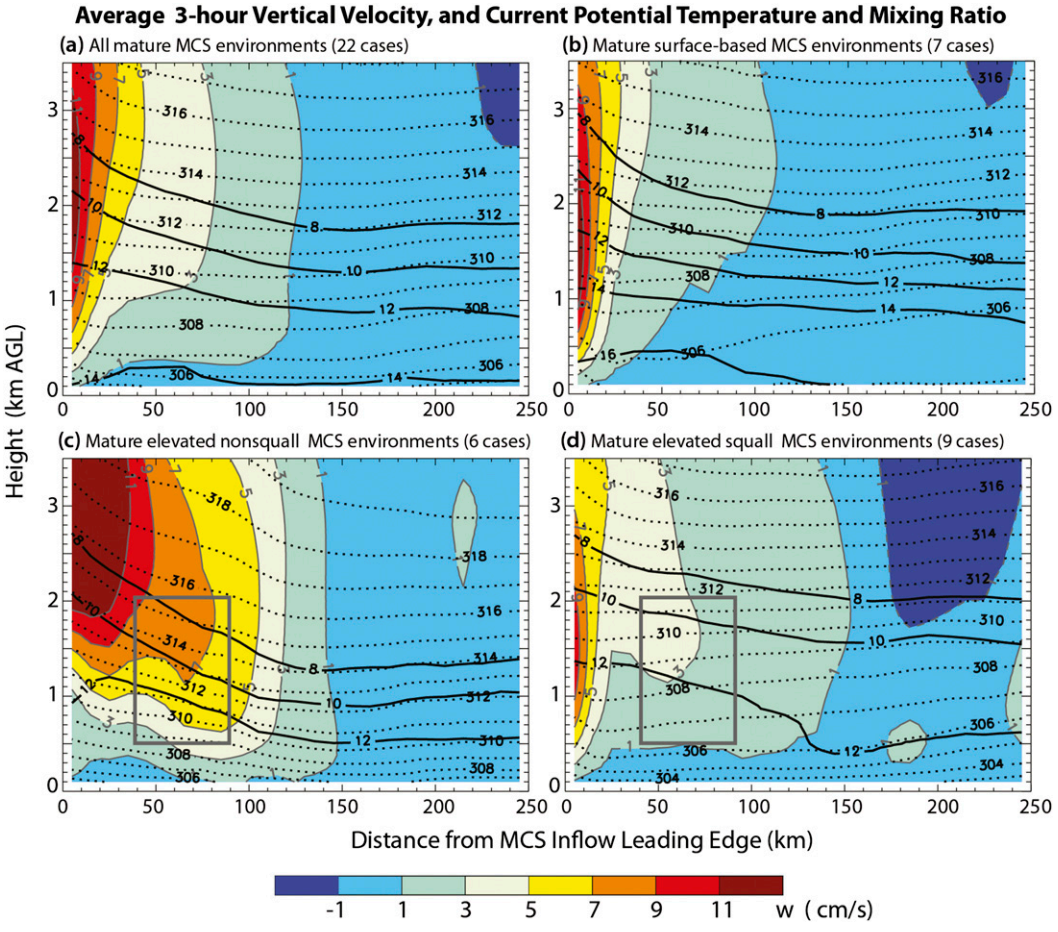

FIG. 13. Average water vapor mixing ratio (black contours starting at 8 g kg^{-1} with 2 g kg^{-1} intervals) and potential temperature (dotted contours with 1-K intervals) at the time of MCS maturity and vertical velocity time averaged for 3 h ending at MCS maturity for environments of (a) all mature MCSs, (b) surface-based MCSs, (c) elevated nonsquall MCSs, and (d) elevated squall MCSs. As in Figs. 10 and 11, these fields are averaged along the width between the two parallel dashed lines in Fig. 6 and within 10-km-distance bins in the direction normal to the local MCS leading-edge location at maturity. The rectangular regions in (c) and (d) indicate the locations over which the B_{min} budget calculations presented in Figs. 15–17 are performed.

is influenced by horizontal temperature advection [first term on the right side of (2)], as well as a combination of adiabatic temperature change and vertical temperature advection [second term on the right side of (2)]. Readers are referred to Part I (section 4) for the mathematical specification of these forcing terms on the right sides of (1) and (2) and discussion of how they are linked to buoyancy changes.

In addition to time averaging for the 3-h period, the budget calculations are area averaged over the width between the parallel dashed lines of individual cases in Fig. 6 within the portion of their inflow region delineated by the rectangles from $r = 40$ to 90 km in panels (c) and (d) in Figs. 10–13. Our reason for using this region 40–90 km ahead of the MCS leading edge is that it avoids outflow boundary circulations, which may extend for a few tens of kilometers beyond the cold-pool boundary (Weisman and Rotunno 2004; Bryan et al. 2012) and diabatic effects, not accounted for in our budget calculations, that result from vertical variations of evaporation that can reduce lower-tropopospheric negative buoyancy over similar distances in MCSs with forward anvils (Parker and Johnson 2004). Together, these effects could conceivably influence the continued decrease in negative buoyancy magnitudes from $r = 40$ to 0 km (Figs. 10c,d). However, we are most interested in diagnosing the more predictable mesoscale thermodynamic forcing factors influencing B_{min}, and B_{min} from $r = 40$ to 90 km is still significantly modified from far-field values beyond $r > 150$ km (Figs. 10c,d).

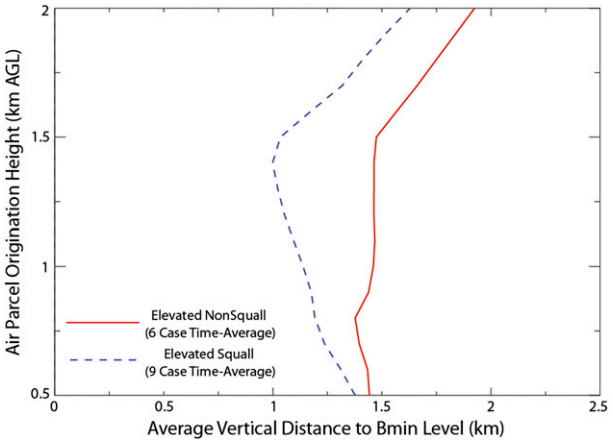

FIG. 14. Average vertical displacements needed to reach their level of minimum buoyancy for air parcels at their indicated origination heights during the 3-h period leading up to MCS maturity for areas of the elevated nonsquall and elevated squall environments within the rectangular regions of Figs, 10c, 11c, 12c, and 13c and Figs. 10d, 11d, 12d, and 13d, respectively.

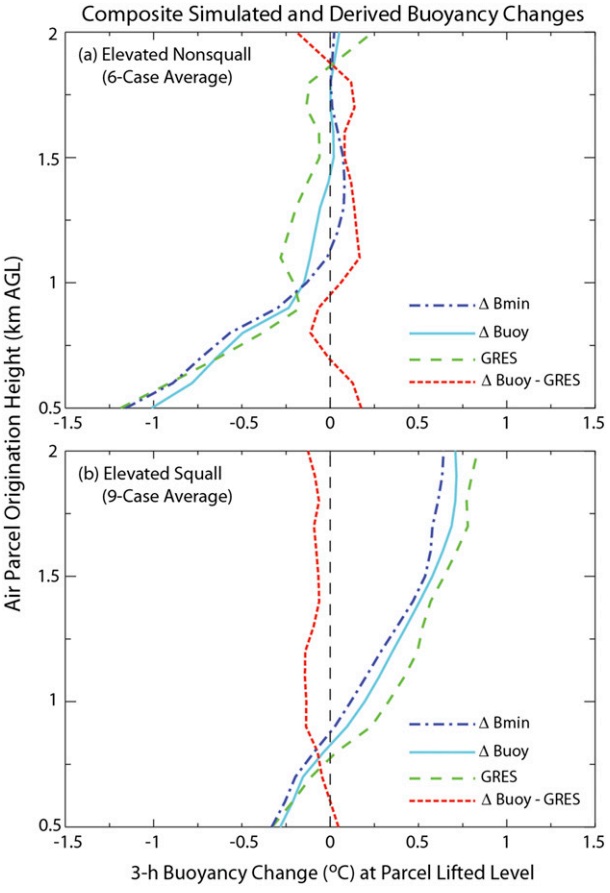

FIG. 15. Budgets diagnosing area-averaged GRES for ΔBuoy at parcel lifted levels that are averages of those of the minimum buoyancy during the 3-hour period, for air parcels at their indicated origination levels for environments of the (a) elevated nonsquall and (b) elevated squall composites. The vertical displacements between the parcel origination heights and the parcel lifted levels are shown in Fig. 14 and the region of horizontal averaging is indicated by the rectangles in Figs. 10c,d; 11c,d; 12c,d; and 13c,d. The actual area-averaged minimum buoyancy changes that ΔBuoy approximates are indicated by ΔBmin. The budget error is indicated by the dashed red curves.

b. *Budget results*

The temporal and area averages of vertical displacements of air parcels from their origination levels to the average level of minimum buoyancy are shown for the ENS and ES composites in Fig. 14. It should be kept in mind that in subsequent plots the vertical axis represents the parcel origination level, and the actual level at which ΔBUOY occurs is obtained by adding these vertical displacements from Fig. 14.

The greater vertical displacement required to reach $B_{\min}$ in the ENS environments (Fig. 14) is a notable difference between the ES and ENS MCS categories. In the absence of strong static stability, parcel $B_{\min}$ levels typically occur near the parcel's lifted condensation level. Thus, the greater vertical displacements necessary to reach $B_{\min}$ in the ENS composite reflect smaller average relative humidities in the ENS cases than in the ES cases. Note that within the rectangular budget region of the ENS composite (Fig. 13c) conditions are both potentially warmer and drier than in the corresponding region of the ES composite (Fig. 13d), which leads to lower relative humidity.

There is good agreement between the time-averaged GRES and 3-h ΔBUOY that it is intended to diagnose for both the ENS (Fig. 15a) and ES composites (Fig. 15b), which is evident from the acceptably small budget residuals (ΔBUOY − GRES) for each composite. Moreover, as in Part I, ΔBUOY is a good approximation to the actual 3-h $B_{\min}$ tendency ΔBMIN (Fig. 15). As a result, the greater total forcing (parcel + environment) for buoyancy increases in the ES composite (Fig. 16b) compared to the ENS composite (Fig. 16a) is consistent with a comparison between the composites of average 3-h $B_{\min}$ changes over the rectangular region in Figs. 11c,d.

As in Part I, the total forcing is subdivided into forcing terms associated with vertical motion (VERTVEL= $\mathrm{VTADV}_P + \mathrm{VMADV}_P + \mathrm{VTADV}_E$), horizontal temperature advection ($\mathrm{HTADV} = \mathrm{HTADV}_P + \mathrm{HTADV}_E$), and horizontal moisture advection ($\mathrm{HMADV} = \mathrm{HMADV}_P$). These terms have contributions from changes to the parcel (Figs. 16c,d) and from changes to the environment at the level to which the parcel is lifted (Figs. 16e,f). In both the ENS and ES composites the collective effects of environmental changes (Figs. 16e,f) have a greater impact in reducing the negative buoyancy than do collective effects of parcel changes (Figs. 16c,d).

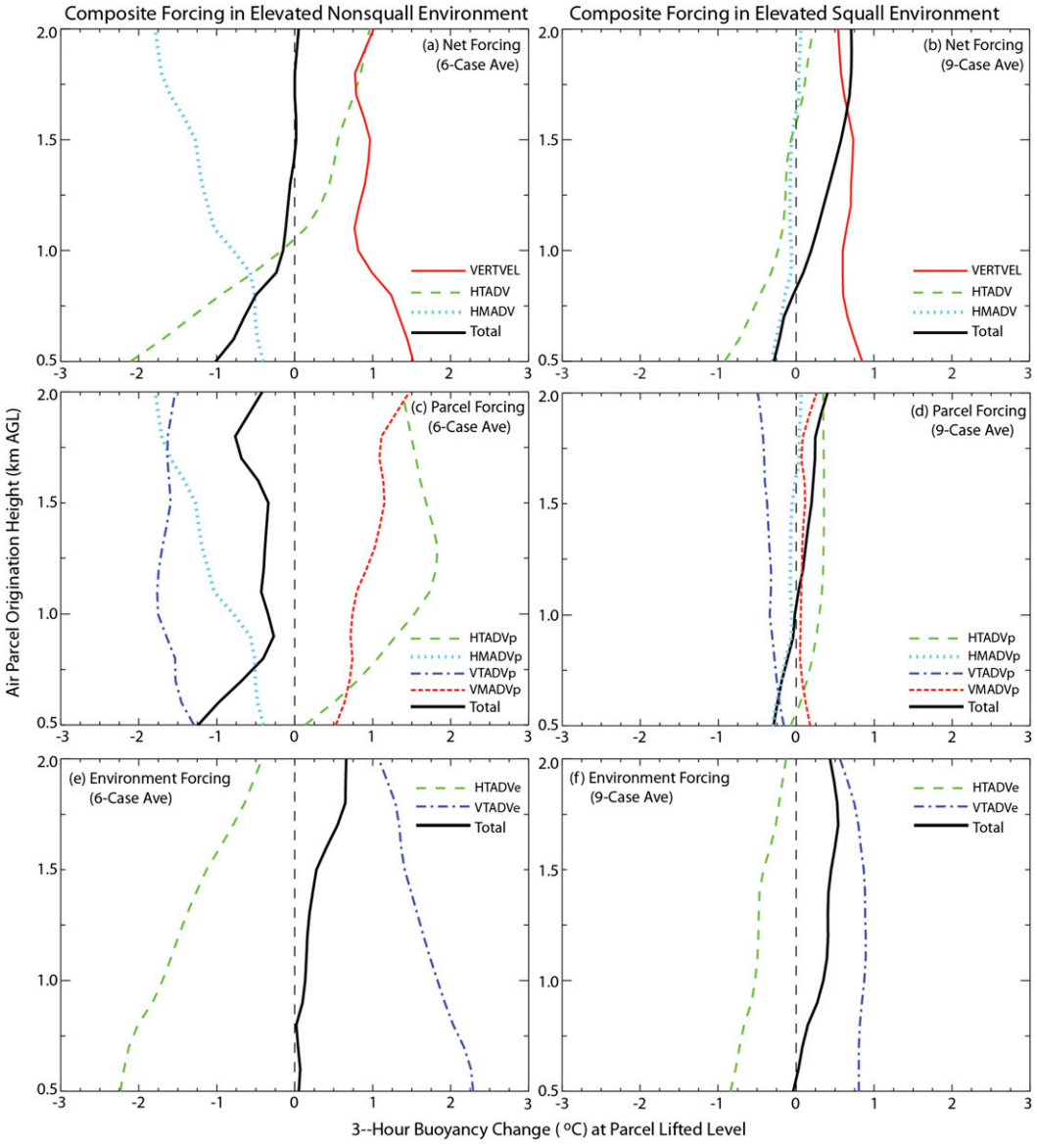

FIG. 16. Composite of budget calculations diagnosing the 3-h time-averaged (a),(b) net contributions to the total forcing for air parcel buoyancy changes at the parcel lifted level for air parcels originating at the indicated levels in the elevated nonsquall and the elevated squall environments for area averages within the rectangles in Figs. 10c, 11c, 12c, and 13c and Figs. 10d, 11d, 12d, and 13d, respectively. The total forcing indicated by the solid black curves in these panels results from the combined effects of both parcel and environmental changes due to VERTVEL, HTADV, and HMADV. (c),(d) As in (a),(b), but for only contributions to the part of the forcing for buoyancy changes related to parcel changes at their origination levels. (e),(f) As in (a),(b), but for only contributions to the forcing for buoyancy changes related to environmental changes at the parcel lifted levels.

Of the three total forcing terms, VERTVEL is the most effective at reducing negative buoyancy for both composites (Figs. 16a,b). Here, the combination of cooling in the environment above parcel origination levels from VTADV_E (Figs. 16e,f) and moistening of the parcel through vertical advection from VMADV_P (Figs. 16c,d) offsets the cooling of the parcel from VTADV_P (Figs. 16c,d).

The net effect of horizontal temperature advection (HTADV) on removing negative buoyancy varies significantly with height in the composites (Figs. 16a,b) despite warm advection occurring through the depth of the 0.5–2-km AGL budget regions (Figs. 12c,d). What is most critical for the reduction of negative buoyancy from warm advection are greater changes at the parcel origination level than environmental changes at the level

to which the parcel is lifted. This occurs only for parcels originating in the top half of the budget layer in the ENS composite (Fig. 16a) and is negligible at these altitudes in the ES composite (Fig. 16b).

The differences in total forcing on buoyancy changes in the ENS and ES composites are influenced most strongly by horizontal moisture advection effects on buoyancy changes (HMADV). The increases in negative buoyancy from HMADV offset decreases in negative buoyancy from the combination of VERTVEL and HTADV, resulting in neutral forcing for buoyancy change between 1 and 2 km AGL in the ENS composite (Fig. 16a). In contrast, the negligible HMADV in the ES composite is unable to offset VERTVEL in this layer, which leads to decreases in negative buoyancy (Fig. 16b). One reason why horizontal moisture advection can be such an effective contributor to destabilizing or stabilizing air parcels is that unlike for horizontal temperature advection or vertical velocity, any compensating effects on the environment at the $B_{\min}$ level (located above the parcel source level) are negligible.

Though there are noticeable differences between the ENS and ES environments in their composites for buoyancy changes associated with the net forcings (Figs. 16a,b), substantial variability occurs among individual cases within the composites (Fig. 17). To examine whether there are statistically significant differences among the ENS and ES populations, we apply the Wilcoxin–Mann–Whitney rank-sum test (e.g., Wilks 1995, section 5.3.1), which is resistant to outliers. We find the differences are statistically significant for HMADV (Figs. 17e,f) at the 95% confidence level ($p = 0.029$) but not for VERTVEL (Figs. 17a,b) and HTADV (Figs. 17c,d).

Further examination of the variability of VERTVEL in individual cases indicates that the three largest contributions toward decreases in negative buoyancy from vertical motion effects in the ES category (Fig. 17b) occur in the environments of the largest MCSs of that category (Figs. 6h,r,t). Two of the largest MCSs in the ES category (Figs. 6r,t) were also associated with the strongest environmental 0.5–3.0-km AGL bulk vertical shear ($\Delta U = 15$–$20\ \mathrm{m\ s^{-1}}$) of any of the nine cases in that category (Fig. 8b).

Large vertical displacements at or very close to the leading edge of squall-type MCSs, which RKW predicts under near-optimal conditions with strong low-level shear, may be sufficient to sustain MCSs even without the larger-scale erosion of negative buoyancy diagnosed in the current study. However, the strength of the vertical shear varies significantly in the ES (Fig. 8b) and SB (Fig. 8c) cases. In the weaker shear cases, anticipated large departures from optimal lifting conditions at the MCS leading edge, implied from RKW, suggest a more critical role of the large-scale erosion of negative buoyancy in MCS sustenance.

c. Discussion

An important but yet unexplained characteristic of the $B_{\min}$ budget calculations is the strong cancellations among different forcing terms on the $B_{\min}$ tendency. These cancellations are most pronounced for the ENS environments (Figs. 16c,e) and may be strongly influenced by the conservation of the moist static energy:

$$\frac{d}{dt}(c_p T + gz + L_v q) = 0. \tag{3}$$

Making the approximation of steady conditions in the environment following the mature MCS (i.e., $\delta T/\delta t = \delta q/\delta t = 0$) and assuming all variation occurs along the MCS movement yields

$$U_{\mathrm{rel}}\frac{\partial T}{\partial x} + w(\Gamma - \Gamma_d) + \frac{L_v}{c_p}\left(U_{\mathrm{rel}}\frac{\partial q}{\partial x} + w\frac{\partial q}{\partial z}\right) = 0, \tag{4}$$

where $\Gamma_d = -g/c_p$ and $\Gamma = \partial T/\partial z$ are the dry-adiabatic and actual atmospheric lapse rates, respectively, and U_{rel} is the system-relative horizontal velocity. The approximately steady conditions in the environment moving with the MCS are anticipated given the quasi-steady state of the MCS itself during its mature stage. If the ENS MCSs are also quasi stationary, the ground-relative horizontal flow U may be used to approximate U_{rel} in (4).

The ENS MCSs occur primarily within frontal zones, which Fritsch and Forbes (2001) associate with approximate isentropic ascent in their type-I MCS environments. If the flow is along isentropes, then $(\partial\theta/\partial x)/(\partial\theta/\partial z) \approx w/U_{\mathrm{rel}}$ with $w = -SU_{\mathrm{rel}}$, where $S = -\partial z/\partial x|_\theta$ is the slope of the isentropes. Here, (4) may be rewritten for quasi-stationary MCS environments as

$$-U\left[\frac{\partial T}{\partial x} - S(\Gamma - \Gamma_d) + \frac{L_v}{c_p}\frac{\partial q}{\partial x} - S\frac{L_v}{c_p}\frac{\partial q}{\partial z}\right] = 0. \tag{5}$$

When the slope of the isentropes S is small, the dominant cancellation is between the horizontal temperature and moisture advection terms [terms 1 and 3 on the left side of (5)]. However, for the ENS composite there is significant slope to the isentropes over the budget region (Fig. 13c). This is consistent with cancellation between the temperature and moisture forcing terms in both the horizontal and vertical directions for air parcels originating within the levels of the budget domain (Fig. 16c).

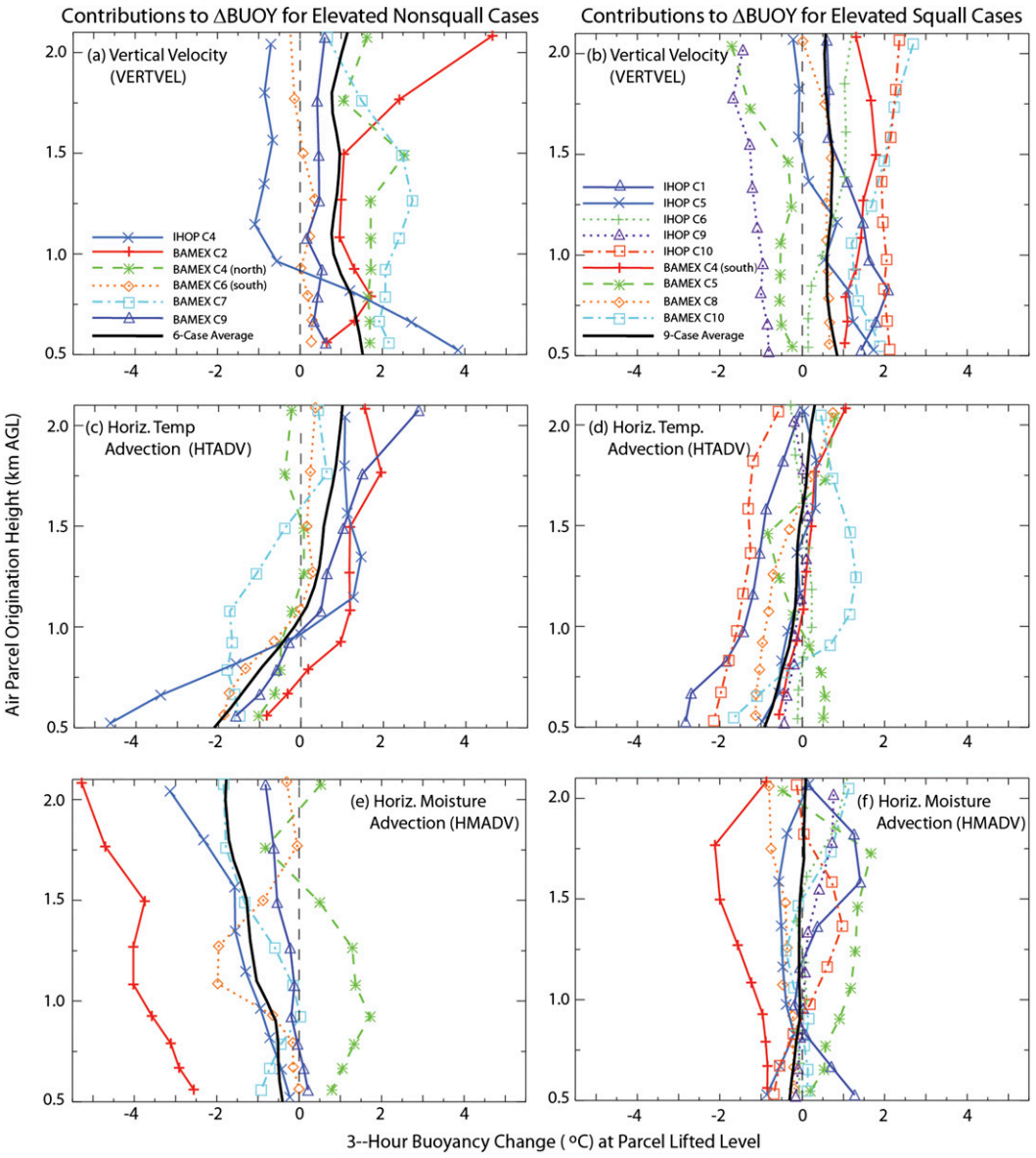

FIG. 17. Forcing terms for the 3-h air parcel buoyancy changes at the parcel lifted level for air parcels originating at the indicated levels for individual cases in the (left) mature elevated nonsquall and (right) elevated squall environment composites shown in Fig. 16. The legends in the top row indicate the individual cases, which are displayed in their mature stages at the end of the 3-h period in Fig. 6.

7. Summary and conclusions

This study uses the parcel buoyancy minimum ($B_{\min}$) to quantify simulated thermodynamic destabilization. In Part I, emphasis was on mesoscale factors influencing convection initiation, whereas in the current study we examine environments of simulated mature MCSs. A major goal of Part I and the current paper has been to quantify physical processes that influence life cycles of MCSs in convection-permitting models. Using $B_{\min}$, which approximates the CIN, simplifies this analysis (Part I) and allows one to view thermodynamic destabilization succinctly as the combination of air parcel changes at their origination levels and environmental changes at levels approximating where minimum buoyancy is attained in the lifted parcels.

In the current study we have composited simulated MCS environments occurring within two different warm-season meteorological regimes that support organized convection over the central United States. The three composite categories, which collectively include 22 mature MCS environments, are formulated considering

different behavioral aspects of the MCSs and include 7 surface-based (SB) and 15 elevated MCS environments where in the latter both the highest-θ_e parcel and the parcel with the largest minimum buoyancy (i.e., the least negative buoyancy) originate from significantly above the surface. The elevated MCS environments, which mature near local midnight (several hours later than the average for SB cases), are further stratified into squall (ES) and nonsquall (ENS) categories based on MCS propagation characteristics.

The ENS MCSs strongly resemble the type-I MCSs classified by Fritsch and Forbes (2001), where convection is sustained in an environment of mesoscale forcing associated with strong warm advection and frontal ascent. In the composite ENS environment, the magnitude of $B_{\min}$ decreases gradually over horizontal scales exceeding 100 km to values indicative of small convective inhibition at the MCS inflow edge. This allows sustained convection even in the absence of strong MCS-induced localized lifting and is not surprising given the strong and persistent mesoscale forcing (e.g., Crook and Moncrieff 1988).

Similar gradual decreases in $B_{\min}$ magnitude toward the MCS inflow edge occur for the ES category and, to a lesser degree, for the SB category. These other environments are less baroclinic than the ENS environments and bear greater resemblance to the environments of type-2 MCSs described by Fritsch and Forbes (2001). The maintenance of this class of MCS is often viewed within the context of the RKW paradigm of strong localized lifting at the MCS-induced outflow. The largest and most intense MCSs (in terms of rainfall) in the ES category have the strongest environmental values of line-normal vertical shear, which supports strong localized lifting through either the RKW mechanism or related mechanisms that are also influenced by near-surface stabilization (e.g., French and Parker 2010). However, the current composite results also indicate weak lifting on scales of ~100 km that help eliminate convection inhibition as an important aspect of MCS maintenance for a wide variety of simulated precipitation systems including squall lines. Weak mesoscale lifting in squall-line environments has also been deduced from recent radiosonde observations (e.g., Bryan and Parker 2010).

Budget calculations of $B_{\min}$ forcing are performed for the ENS and ES environments over the 3-h period during their mature stage. Similar to the case study results of elevated convection initiation reported in Part I, the reduction in lower-tropospheric negative buoyancy is dominated by effects related to vertical motion for both environmental categories. Together, vertical moisture advection increasing parcel humidities and environmental cooling above the parcel origination level, owing to adiabatic temperature changes, more than offset the vertical motion contributions to the negative buoyancy associated with parcel cooling.

Warm advection diagnosed in observationally based composites of large MCSs (e.g., Maddox 1983; Cotton et al. 1989) is a pervasive feature of both the simulated ENS and ES environments. However, herein, its direct effect on reducing negative buoyancy is less than that of vertical motions. Though the warm advection is often enhanced by the vertically confined nocturnal LLJ, it can be significant through relatively deep lower-tropospheric layers. Thus, reductions in $B_{\min}$ magnitudes from parcel warming due to horizontal advections do not always dominate those associated with horizontal advections warming the environment above. In these circumstances the warm advection may play a more significant direct role on MCS maintenance through its effect on CAPE, which is influenced by destabilization through deeper layers.

The budget calculations illustrate not only the importance of the vertical distributions of thermodynamic forcings, but also the importance of offsetting effects from different forcing terms on $B_{\min}$ changes. Despite much larger average upward motion and warm advection in the ENS composite, reductions in $B_{\min}$ magnitude during the MCS mature stage are greater in the ES composite. This results from stabilizing effects of strong negative horizontal moisture advection, which offsets the destabilizing effects of upward motion in the ENS composite. We note that such large cancellations may be influenced by moist static energy conservation (section 6c).

The particularly strong negative horizontal moisture advection in the ENS composite is also a ramification of the large-scale pattern of a quasi-stationary lower-tropospheric baroclinic zone (where the ENS MCSs reside) with hot and relatively dry air on its southern (upstream) side. The persistent local upward motion in the MCS environment within the quasi-stationary frontal zone results in a localized mesoscale deepening of the lower-tropospheric moisture and development of strong horizontal moisture gradients above the surface in the MCS inflow direction. The negative horizontal moisture advection in all but one of the six ENS cases represents the most significant $B_{\min}$ forcing difference between the ENS and ES composites.

An important remaining question concerns how the MCS environment in mature elevated MCS cases is influenced by MCS-induced circulations. In the current $B_{\min}$ budget formulation diabatic effects have been neglected and budget residuals are still acceptably small. However, MCS-related adiabatic changes to the mature

stage environment could still be occurring. While such effects are likely mitigated by our confinement of budget calculations to a zone 40–90 km upstream of the MCS, it is impossible to entirely remove such effects in the current experiment design. Other important topics for future research include examination of how our results could vary with geographical region and time of year. Though the overall characteristics of precipitation are well simulated in the current study, additional studies are needed to determine how closely modeled thermodynamic vertical structures and $B_{\min}$ conform to observations.

Acknowledgments. The authors thank Craig Schwartz (NCAR/MMM) for informative discussions concerning the fractions skill score (FSS). The helpful comments of two anonymous reviewers led to important clarifications in the manuscript. This research was performed as part of NCAR's Short Term Explicit Prediction (STEP) program, which is supported by national science funds for the U. S. Weather Research Program (USWRP).

REFERENCES

Barnes, G. M., and K. Sieckman, 1984: On the environment of fast- and slow-moving mesoscale convective cloud lines. *Mon. Wea. Rev.,* **112,** 1782–1794.

Benjamin, S. B., and Coauthors, 2004: An hourly assimilation–forecast cycle: The RUC. *Mon. Wea. Rev.,* **132,** 495–518.

Bluestein, H., and M. H. Jain, 1985: Formation of mesoscale lines of precipitation: Severe squall lines in Oklahoma during the spring. *J. Atmos. Sci.,* **42,** 1711–1732.

Bryan, G. H., and M. D. Parker, 2010: Observations of a squall line and its near environment using high-frequency rawinsonde launches during VORTEX2. *Mon. Wea. Rev.,* **138,** 4076–4097.

——, R. Rotunno, and M. L. Weisman, 2012: What is RKW theory? *Proc. 26th Conf. on Severe Local Storms,* Nashville, TN, Amer. Meteor. Soc., 4B.6. [Available online at https://ams.confex.com/ams/26SLS/webprogram/Paper211731.html.]

Carbone, R. E., J. D. Tuttle, D. A. Ahijevych, and S. B. Trier, 2002: Inferences of predictability associated with warm-season precipitation episodes. *J. Atmos. Sci.,* **59,** 2033–2056.

Chen, F., Z. I. Janjić, and K. E. Mitchell, 1997: Impact of atmospheric surface layer parameterization in the new land surface scheme of the NCEP mesoscale Eta numerical model. *Bound.-Layer Meteor.,* **85,** 391–421.

——, and Coauthors, 2007: Evaluation of the characteristics of the NCAR high-resolution land data assimilation system during IHOP_2002. *J. Appl. Meteor. Climatol.,* **46,** 694–713.

Colby, F. P., Jr., 1984: Convective inhibition as a predictor of convection during AVE-SESAME II. *Mon. Wea. Rev.,* **112,** 2239–2252.

Coniglio, M. C., S. F. Corfidi, and J. S. Kain, 2012: Views on applying RKW theory: An illustration using the 8 May 2009 derecho-producing convective system. *Mon. Wea. Rev.,* **140,** 1023–1043.

Cotton, W. R., M. S. Lin, R. L. McAnelly, and C. J. Tremback, 1989: A composite model of mesoscale convective complexes. *Mon. Wea. Rev.,* **117,** 765–783.

Crook, N. A., and M. W. Moncrieff, 1988: The effect of large-scale convergence on the generation and maintenance of deep moist convection. *J. Atmos. Sci.,* **45,** 3606–3624.

Davis, C. A., and Coauthors, 2004: The Bow-Echo and MCV Experiment. *Bull. Amer. Meteor. Soc.,* **85,** 1075–1093.

Dudhia, J., 1989: Numerical study of convection observed during the Winter Monsoon Experiment using a mesoscale two-dimensional model. *J. Atmos. Sci.,* **46,** 3077–3107.

Ek, M. B., K. E. Mitchell, Y. Lin, E. Rogers, P. Grummann, V. Koren, G. Gayno, and J. D. Tarpley, 2003: Implementation of Noah land surface model advances in the National Centers for Environmental Prediction operational mesoscale Eta model. *J. Geophys. Res.,* **108,** 8851, doi:10.1029/2002JD003296.

Fovell, R. G., 2002: Upstream influence of numerically simulated squall-line storms. *Quart. J. Roy. Meteor. Soc.,* **128,** 893–912.

French, A. J., and M. D. Parker, 2010: The response of simulated nocturnal convective systems to a developing low-level jet. *J. Atmos. Sci.,* **67,** 3384–3408.

Fritsch, J. M., and G. S. Forbes, 2001: Mesoscale convective systems. *Severe Convective Storms, Meteor. Monogr.,* No. 50, Amer. Meteor. Soc., 323–357.

Fulton, R. A., J. P. Breidenbach, D.-J. Seo, D. A. Miller, and T. O'Bannon, 1998: The WSR-88D rainfall algorithm. *Wea. Forecasting,* **13,** 377–395.

Houze, R. A., Jr., B. F. Smull, and P. Dodge, 1990: Mesoscale organization of springtime rainstorms in Oklahoma. *Mon. Wea. Rev.,* **118,** 613–654.

Janjić, Z. I., 2002: Nonsingular implementation of the Mellor–Yamada level 2.5 scheme in the NCEP Meso model. NCEP Office Note 437, 61 pp. [Available online at http://www.emc.ncep.noaa.gov/officenotes/newernotes/on437.pdf.]

Johns, R. H., and W. D. Hirt, 1987: Derechos: Widespread convectively induced windstorms. *Wea. Forecasting,* **2,** 32–49.

Kane, R. J., Jr., C. R. Chelius, and J. M. Fritsch, 1987: Precipitation characteristics of mesoscale convective weather systems. *J. Climate Appl. Meteor.,* **26,** 1345–1357.

LeMone, M. A., E. J. Zipser, and S. B. Trier, 1998: The role of environmental shear and thermodynamic conditions in determining the structure and evolution of mesoscale convective systems during TOGA COARE. *J. Atmos. Sci.,* **55,** 3493–3518.

Maddox, R. A., 1980: Mesoscale convective complexes. *Bull. Amer. Meteor. Soc.,* **61,** 1374–1387.

——, 1983: Large-scale meteorological conditions associated with midlatitude mesoscale convective complexes. *Mon. Wea. Rev.,* **111,** 1475–1493.

——, C. F. Chappell, and L. R. Hoxit, 1979: Synoptic and meso-α scale aspects of flash flood events. *Bull. Amer. Meteor. Soc.,* **60,** 115–123.

——, K. W. Howard, D. L. Bartels, and D. M. Rodgers, 1986: Mesoscale convective complexes in the middle latitudes. *Mesoscale Meteorology and Forecasting,* P. Ray, Ed., Amer. Meteor. Soc., 390–413.

McAnelly, R. L., and W. R. Cotton, 1989: The precipitation life cycle of mesoscale convective complexes over the central United States. *Mon. Wea. Rev.,* **117,** 784–808.

Mlawer, E. J., S. J. Taubman, P. D. Brown, M. J. Iacono, and S. A. Clough, 1997: Radiative transfer for inhomogeneous atmosphere: RRTM, a validated correlated-k model for the longwave. *J. Geophys. Res.,* **102** (D14), 16 663–16 682.

Parker, M. D., 2008: Response of simulated squall lines to low-level cooling. *J. Atmos. Sci.,* **65,** 1323–1341.

——, and R. H. Johnson, 2004: Simulated convective lines with leading precipitation. Part II: Evolution and maintenance. *J. Atmos. Sci.,* **61,** 1656–1673.

Roberts, N. M., and H. W. Lean, 2008: Scale-selective verification of rainfall accumulations from high-resolution forecasts of convective events. *Mon. Wea. Rev.,* **136,** 78–97.

Rotunno, R., J. B. Klemp, and M. L. Weisman, 1988: A theory for strong, long-lived squall lines. *J. Atmos. Sci.,* **45,** 1990–2013.

Schumacher, R. S., and R. H. Johnson, 2008: Mesoscale processes contributing to extreme rainfall in a midlatitude warm-season flash flood. *Mon. Wea. Rev.,* **136,** 3964–3986.

Schwartz, C. S., and Coauthors, 2009: Next-day convection allowing WRF model guidance: A second look at 2-km versus 4-km grid spacing. *Mon. Wea. Rev.,* **137,** 3351–3371.

Skamarock, W. C., and J. B. Klemp, 2008: A time-split nonhydrostatic atmospheric model for weather research and forecasting applications. *J. Comput. Phys.,* **227,** 3465–3485.

Sun, J., S. B. Trier, Q. Xiao, M. L. Weisman, H. Wang, Z. Ying, M. Xu, and Y. Zhang, 2012: Sensitivity of 0–12-h warm-season precipitation forecasts over the central United States to model initialization. *Wea. Forecasting,* **27,** 832–855.

Thompson, G., P. R. Field, R. M. Rasmussen, and W. D. Hall, 2008: Explicit forecasts of winter precipitation using an improved bulk microphysics scheme. Part II: Implementation of a new snow parameterization. *Mon. Wea. Rev.,* **136,** 5095–5115.

Trier, S. B., C. A. Davis, D. A. Ahijevych, M. L. Weisman, and G. H. Bryan, 2006: Mechanisms supporting long-lived episodes of propagating nocturnal convection within a 7-day WRF model simulation. *J. Atmos. Sci.,* **63,** 2437–2461.

——, M. A. LeMone, F. Chen, and K. W. Manning, 2011a: Effects of heat and moisture exchange on ARW-WRF warm-season precipitation forecasts over the central United States. *Wea. Forecasting,* **26,** 3–25.

——, J. H. Marsham, C. A. Davis, and D. A. Ahijevych, 2011b: Numerical simulations of the postsunrise reorganization of a nocturnal mesoscale convective system during 13 June IHOP_2002. *J. Atmos. Sci.,* **68,** 2988–3011.

——, C. A. Davis, D. A. Ahijevych, and K. W. Manning, 2014: Use of the parcel buoyancy minimum ($B_{\min}$) to diagnose simulated thermodynamic destabilization. Part I: Methodology and case studies of MCS initiation environments. *Mon. Wea. Rev.,* **142,** 945–966.

Tuttle, J. D., and C. A. Davis, 2006: Corridors of warm season precipitation in the central United States. *Mon. Wea. Rev.,* **134,** 2297–2317.

Wallace, J. M., 1975: Diurnal variations in precipitation and thunderstorm frequency over the conterminous United States. *Mon. Wea. Rev.,* **103,** 406–419.

Weckwerth, T. M., and Coauthors, 2004: An overview of the International H_2O Project (IHOP_2002) and some preliminary highlights. *Bull. Amer. Meteor. Soc.,* **85,** 253–277.

Weisman, M. L., and R. Rotunno, 2004: ''A theory for strong long-lived squall lines'' revisited. *J. Atmos. Sci.,* **61,** 361–382.

Wilks, D. S., 1995: *Statistical Methods in the Atmospheric Sciences.* Academic Press, 467 pp.